

# Coherent Control of Quantum Information

by

Michael Kevin Henry, Jr.

Submitted to the Department of Nuclear Science and Engineering  
in partial fulfillment of the requirements for the degree of  
Doctor of Philosophy in Nuclear Science and Engineering

at the

MASSACHUSETTS INSTITUTE OF TECHNOLOGY

June 2007

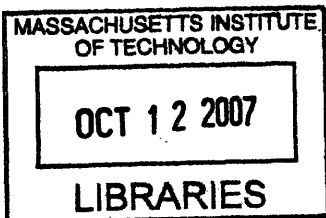
© Massachusetts Institute of Technology 2007. All rights reserved.

Author .....  
Department of Nuclear Science and Engineering  
April 30, 2007

Certified by .....  
David G. Cory  
Professor  
Thesis Supervisor

Read by .....  
Alan Jasanoff  
Assistant Professor

Accepted by .....  
Jeffrey A. Coderre  
Chairman, Department Committee on Graduate Students



ARCHIVES



# Coherent Control of Quantum Information

by

Michael Kevin Henry, Jr.

Submitted to the Department of Nuclear Science and Engineering  
on April 30, 2007, in partial fulfillment of the  
requirements for the degree of  
Doctor of Philosophy in Nuclear Science and Engineering

## Abstract

Quantum computation requires the ability to efficiently control quantum information in the presence of noise. In this thesis, NMR quantum information processors (QIPs) are used to study noise processes that compromise coherent control, to develop useful techniques for detecting noise, and to explore effective noise-protection schemes.

A quantum simulation of the quantum sawtooth map in the perturbative parameter regime is used to study the effects of experimental noise on quantum localization, a highly sensitive quantum interference phenomenon that depends on the coherence of the localized state. Experimental data and numerical simulations show that the decoherent noise known to act on the system is relatively inconsequential in this implementation of the map, and that incoherent noise is the biggest challenge to implementing localization.

While many incoherent processes appear decoherent, there are important differences. The distribution functions underlying incoherent processes are either static or slowly varying and so the errors introduced by these distributions are refocusable. The influence of incoherent noise is further explored in an experimentally implemented entangling operation, where incoherence can be difficult to separate from decoherence. By studying the fidelity decay under the cyclic entangling map, the effects of incoherence are easily distinguished from decoherence in experimental data.

Decoherence free subspaces (DFSs) provide some of the most efficient schemes of avoiding decoherence from noise sources with underlying symmetries. To achieve an internal Hamiltonian structure that naturally fits a DFS encoding over a well-defined Hilbert space, we employ liquid crystal solvents to partially align a four-proton spin system, reintroducing the spin-spin dipolar couplings. In these experiments, enhanced coherent control is achieved by encoding logical qubits in a DFS. Robust control sequences enable high fidelity control in the DFS even when the system Hamiltonian is known with some uncertainty.

Thesis Supervisor: David G. Cory  
Title: Professor



## Acknowledgments

I would like to thank David Cory for giving me the opportunity to work with him and the Cory group, and for all of the advice and instruction David has given during my years as a graduate student. David's integrity, energy, wisdom and kindness have truly inspired me.

I am thankful to many research collaborators and friends who contributed to the work described in this thesis - Sekhar Ramanathan, Joseph Emerson, Jonathan Hodges, Paola Cappellaro, Nicolas Boulant, Yaakov Weinstein, Alexey Gorshkov, Tim Havel, Colm Ryan, Mike Ditty, and Rudy Martinez.

I would also like to thank other Cory group members whom I have had the pleasure of working with - Deborah Chen, Jennifer Choy, Matthew Davidson, Anatoly Dementyev, Louis Fernandes, Daniel Greenbaum, Kai Iamsung, Benjamin Levi, Cecilia Lopez, T. S. Mahesh, Kota Murali, Dmitry Pushin, Suddha Sinha, and Sergio Valenzuela. Special thanks to Jamie Yang, Troy Borneman and Hyungjoon Cho for helping out with many successful helium fills.

I am especially thankful to my very good friends and co-members of Graduate Lunch Seminar - Jamie Yang, Leeland Ekstrom, Alex Ince-Cushman, and Jonathan Hodges. Memories of quizbowl and our weekly meetings at Sunny's will always be dear to me.

I would like to thank my friends and family at home in Texas and in Colorado for their support and encouragement. Words cannot express my gratitude for my loving wife Brook, whose endless patience, kindness, and encouragement have been my source of strength and happiness through graduate school. Finally, I am thankful to God my Creator for His grace through Christ and for a life of abundant blessing.



*Dedicated to my wife Brook,  
“... the only one I see.”*





# Contents

<b>1</b>	<b>Introduction</b>	<b>17</b>
1.1	Quantum information processors . . . . .	18
1.2	Toward more qubits and larger systems . . . . .	19
<b>2</b>	<b>Localization in the quantum sawtooth map</b>	<b>21</b>
2.1	The sawtooth map . . . . .	23
2.2	Implementation details . . . . .	26
2.3	Numerical simulation . . . . .	32
2.4	Experimental results . . . . .	36
2.5	Discussion . . . . .	37
2.6	Conclusions . . . . .	42
<b>3</b>	<b>Signatures of incoherence</b>	<b>43</b>
3.1	Identifying incoherence by fidelity decay . . . . .	44
3.1.1	Decoherent noise . . . . .	45
3.1.2	Incoherent noise . . . . .	47
3.2	Experiment . . . . .	49
3.3	Numerical simulation . . . . .	51
3.4	Results and discussion . . . . .	54
3.5	Conclusions . . . . .	57
<b>4</b>	<b>Liquid crystal solvent NMR QIPs</b>	<b>59</b>
4.1	NMR with liquid crystal solvents . . . . .	59
4.2	Dipolar coupling in a partially oriented system . . . . .	62
4.3	Liquid crystal solvent NMR QIPs . . . . .	65

<b>5</b>	<b>Enhanced control by logical qubit encoding</b>	<b>71</b>
5.1	System model . . . . .	71
5.2	Experiment . . . . .	74
5.3	Analysis . . . . .	77
5.4	Conclusions . . . . .	79
<b>6</b>	<b>Future direction</b>	<b>81</b>
6.1	Larger Hilbert spaces . . . . .	81
6.2	Limited addressability . . . . .	82
6.3	Complex dynamics . . . . .	83
6.4	Conclusions . . . . .	83
<b>A</b>	<b>Fidelity of logical qubit control</b>	<b>87</b>
A.1	Measures of control . . . . .	87
A.2	Control in the logical subspace . . . . .	89

# List of Figures

2-1	The momentum distribution after 0, 5, 10, and 40 iterations of the classical and quantum sawtooth maps. The classical map is chaotic, which causes the distribution to diffusively broaden. The quantum map causes localization, and the breadth of the distribution is essentially static. . . . .	25
2-2	Quantum circuits for implementing the quantum sawtooth map: the quantum Fourier transform and a generalized diagonal unitary operator. These circuits enable a computationally efficient quantum simulation of the quantum sawtooth map. . . . .	27
2-3	A diagram of the tris(trimethylsilyl)silane-acetylene molecule used to simulate the quantum sawtooth map in a liquid state NMR QIP. . . . .	30
2-4	The hydrogen and carbon rf control fields versus time for the full quantum sawtooth map pulse sequence. . . . .	31
2-5	The nine point distribution of carbon rf powers measured in previous experiments and used to simulate the experimentally implemented control sequence for the quantum sawtooth map. . . . .	34
2-6	Momentum distributions for different regions of the ensemble generated by numerical simulations of the experiment which account for T1 and T2 decoherence. Each plot represents the momentum distribution resulting from a numerical simulation of the control sequence with a different carbon rf power. In experiments, the weighted average over the incoherence is observed. . . .	35
2-7	The momentum distribution observed in the experiment and in various numerical simulations of the experiment after zero through three iterations of the quantum sawtooth map. . . . .	36

2-8	The full width at half maximum (FWHM) of the momentum distribution after zero through four iterations of the sawtooth map in various implementations. The FWHM reveals that despite the noise affecting the QIP, the distribution mimics the ideal quantum behavior, and does not diffusively broaden as in the classical case. . . . .	38
2-9	The second moment of the momentum distribution determined from numerical simulations of the quantum sawtooth map experiment including the error models discussed in the text, compared to the ideal data and the experimental data. This plot demonstrates the relative importance of the individual noise mechanisms as they contribute to the experimentally observed delocalization process. . . . .	39
2-10	The magnitude of each element of the superoperators and most significant Kraus operators for numerical simulations of the quantum sawtooth map experiment, including different types of errors. . . . .	41
3-1	The quantum circuit for exploring incoherence in an entangling operation on a QIP. The circuit creates a maximally entangled GHZ state, to which $4n$ iterations of a two-qubit entangling operation are applied. The resulting entangled state is then converted to a computational basis state. . . . .	50
3-2	A diagram of the tris(trimethylsilyl)silane-acetylene molecule used to implement the quantum circuit in Fig. 3-1 in a liquid state NMR QIP. . . . .	51
3-3	The distribution of carbon rf powers measured in previous experiments and used in numerical simulations of the NMR implementation of the circuit in Fig. 3-1. . . . .	52
3-4	The fidelity decay from a numerical simulation of the experiment, where rf inhomogeneity is simulated using two different models. Comparison of the two plots shows that the fidelity decay recurrences are caused by incoherent noise. . . . .	53
3-5	The sum of the absolute value of the density matrix components measured in the experiment and in numerical simulations. This plot shows that incoherence in the entangling operation appears with distinct signatures in the experimental data. . . . .	55

3-6	The Fourier transform of each experimentally measured component of the density matrix, compared to numerical simulations of the experiment using two models of rf inhomogeneity discussed in the text. This plot shows that incoherence in the experimentally implemented entangling operation appears as high frequency components in the Fourier transform of a state fidelity measurement. . . . .	56
4-1	Illustration of the order properties of a nematic liquid crystal phase, showing orientational but not positional ordering. Solutes dissolved in a nematic liquid crystal adopt preferred orientations that restrict thermal rotation, causing nuclear spins within the molecule to retain non-zero dipolar interactions which are not present in an isotropic liquid. . . . .	60
4-2	600 MHz proton spectrum of o-chloronitrobenzene (CNB) partially oriented by the liquid crystal solvent ZLI-1132 showing suppression of the baseline signal caused by the solvent material. The baseline is suppressed by the Cory-48 pulse sequence, parameterized to refocus the dipolar couplings among solute protons but not among solvent protons. . . . .	61
4-3	Coordinate frames used in the expression of the order parameter, which determines the intramolecular nuclear spin dipolar coupling strengths. . . . .	63
4-4	600 MHz proton spectrum of benzene partially oriented by the liquid crystal solvent ZLI-1132. . . . .	65
4-5	Comparison of three regimes of NMR QIP, showing liquid crystal solvent NMR QIPs (LNQs) as a bridge between liquid and solid state implementations. LNQs provide a natural setting for addressing some of the important challenges in solid state NMR quantum information processing. . . . .	67
5-1	600 MHz proton spectrum of o-chloronitrobenzene (CNB) partially oriented by the liquid crystal solvent ZLI-1132. The inset was collected under the MREV-8 sequence, and shows the four protons uncoupled with chemical shifts scaled by the average Hamiltonian. . . . .	74

5-2	The procedure and experimental results of creating a Bell state over two logical qubits encoded in the four dipolar-coupled protons of the CNB molecule. The experimentally prepared logical input state has a correlation of 0.90 with the numerically simulated logical input state. The correlation for the Bell states is 0.84. . . . .	76
5-3	Correlation of the numerically simulated and experimentally measured density matrices for the logical input state and the logical Bell state. The correlations are averaged over a dispersion of simulated Hamiltonian parameters. As more couplings are varied, the correlations decrease only slightly since the pulse sequences were engineered to be robust to these variations, and the loss in correlation is most pronounced for the input state. . . . .	78
5-4	Fidelity of two-qubit entangling operation pulses numerically simulated under various conditions, comparing control of two logical qubits versus all pairs of spin qubits. The fidelity under each set of conditions is significantly better in the case of logical qubits than for any pair of spin qubits. . . . .	79
6-1	Diagram of the 4-hydroxyphenanthrene molecule which could be used as a 16 qubit heteronuclear LNQ. . . . .	82
6-2	NMR spectra for different regimes of Hamiltonians, showing addressable spins in the liquid state, resolved spin transitions in partially oriented systems, and many equivalent spins broadened by dipolar interactions in a solid. . . . .	84

# List of Tables

2.1	Pulse sequence data for the quantum sawtooth map. . . . .	31
-----	---	----





# Chapter 1

## Introduction

Quantum systems have unique properties that are not observed in the classical, macroscopic world. Information stored in a quantum system - “quantum information” - has inherent manifestations of these unique properties and therefore has capabilities that are unparalleled in traditional computing devices. A quantum computer harnesses the computational power of quantum systems, exploiting coherent superposition states, entanglement, and other quantum resources, to achieve an advantage over classical computers in solving certain problems, such as factoring large numbers and searching unsorted lists [42, 95]. The feasibility of quantum computation relies on the possibility of quantum error encodings [96, 100], which enable arbitrarily precise quantum computation in the presence of noise [59].

In perhaps its most important function, a quantum computer can be programmed to simulate the dynamics of other quantum systems [36, 71]. Efficient quantum algorithms have been found for simulating a variety of complex quantum systems [1, 2, 40, 69, 93]. In this capacity, quantum computers could provide meaningful insight into the dynamics of large quantum systems which cannot be efficiently simulated on classical computers. In the second chapter of this thesis, an experimental implementation of one such algorithm [7] which efficiently simulates the dynamics of the quantum sawtooth map is presented.

The criteria [30] necessary for utilizing the full power of quantum computation have not currently been realized in any device. However, quantum information processors (QIPs) provide an experimentally accessible means for exploring coherent quantum control and for implementing quantum algorithms. This thesis describes a number of experiments performed with nuclear magnetic resonance (NMR) QIPs. The ideas explored in these ex-

periments have application in ongoing efforts to engineer precise coherent control in larger systems, toward a scalable quantum computer. The QIPs used here operate with a small number of quantum bits (qubits) in highly mixed states, and they are subject to significant noise.

## 1.1 Quantum information processors

Experimental implementations of quantum information processing have developed in a number of technologies including liquid state NMR, which allows precise coherent control of small networks of weakly coupled nuclear spins. Liquid state NMR experiments mimic pure state quantum dynamics by utilizing isomorphic pseudopure states [20, 41]. This approach has been used to successfully implement a variety of quantum information concepts including quantum error correction [11, 23], the Deutsch-Jozsa algorithm [50], the quantum Fourier transform [117], Shor's factoring algorithm [108], quantum process tomography [115], noiseless subsystems [38, 110], decoherence free subspaces [37, 49], various simulations of quantum dynamics [17, 98, 107, 116], and studies of quantum entanglement [9, 105] including experiments with up to twelve qubits [81].

A number of approaches have been developed for reducing the effects of noise in QIPs, advancing the state of the art in these devices. Strongly modulating pulses (SMPs) are numerically optimized rf control fields which implement precise, spin-selective control, averaging out all unwanted time evolution in the system while minimizing the effects of decoherence [37]. Gradient ascent pulse engineering (GRAPE) has also been used to design numerically optimized pulse sequences which implement precise unitary operators [54]. In addition, quantum error-correcting codes [96, 100], noiseless subsystems [58, 122], decoherence free subspaces [32, 70, 122], dynamical decoupling [109, 111–113], composite pulses [24, 68], and robust pulses [88], have all been developed for protecting quantum information against noise and decoherence. The noise protection scheme most appropriate for a given system is generally determined by the noise model, since each scheme is best suited for certain types of noise. In Chapter Three of this thesis, a discussion of incoherent noise is presented, along with a method for identifying its presence in a QIP, so that the appropriate noise protection scheme may be chosen.

## 1.2 Toward more qubits and larger systems

While liquid state NMR systems provide a useful testbed for quantum computation and continue to yield meaningful progress, they are fundamentally limited in their scalability - their potential to efficiently incorporate more qubits. As the number of qubits in a liquid state NMR QIP increases, the signal decreases exponentially [114]. Many of the proposed scalable approaches to nuclear spin-based quantum computing envision solid state implementations [21, 52, 55, 62, 94, 101]. Solids are composed of large networks of dipolar-coupled nuclear spins, and a principal challenge in these systems is controlling the multispin dynamics. While methods for coherent control of solid state nuclear spin systems have progressed [4, 5, 89], incorporating all the desired capabilities of a quantum computer remains a challenge.

Liquid crystal solvent NMR QIPs [72, 120] provide an intermediate ground between liquid and solid state implementations. Molecules dissolved in liquid crystalline material contain networks of dipolar-coupled spins that, to a good approximation, are uncoupled from their environment [34]. The network of spins is effectively limited to single molecules, and each spin in a molecule may have a unique resonance frequency, thus the multispin dynamics are more easily controlled than in solids. While liquid crystal solvent NMR QIPs are not scalable, they do present the possibility of modestly increasing the size of experimentally accessible Hilbert spaces, since interactions are mediated by strong long-range dipolar couplings and are not limited to bond-mediated scalar couplings as in liquids. Liquid crystals offer a more tractable setting for studying dipolar-coupled spin networks, while maintaining sufficient complexity to provide meaningful contributions to scalable systems.

The second section of this thesis has three parts: Chapter Four introduces fundamentals of liquid crystal solvent NMR QIPs, Chapter Five describes an implementation of two logical qubits using this technology, and Chapter Six suggests a future direction of these studies and how they might contribute to progress in the broader efforts of the quantum computing community.



## Chapter 2

# Localization in the quantum sawtooth map

The development of quantum computers promises a new approach for exploring quantum mechanics in complex systems. In the future, we hope to use quantum computation to emulate quantum behavior in Hilbert spaces that are larger than can be simulated on a classical computer. Today we have access to QIPs that are prototypes of quantum computers (QCs). These devices operate over small and limited Hilbert spaces, and with significant noise. However, even with these limitations they can be used to explore questions of quantum mechanics that start to reflect the power we expect of future QCs. Even when QIPs operate on highly mixed states, as is the case for liquid state NMR implementations, we can distill properties that are consistent with the desired quantum phenomena. Here we will explore one such example, localization under the quantum sawtooth map. Localization is a uniquely quantum phenomenon and thus a natural target of quantum computation.

Dynamical localization occurs in classically chaotic quantum maps, in which the quantum state initially diffuses at the classical rate due to repeated quasi-random perturbations, but then stabilizes to a fixed probability distribution and remains coherently localized under subsequent perturbations [16]. In the case of perturbative localization, the probability distribution is localized with no initial period of diffusion. In both cases, the exponentially peaked, static probability distribution distinctly contrasts with the classical, diffusive behavior. Efficient algorithms have been developed for simulating the dynamics of localization in the kicked rotator model [39], the quantum sawtooth map [7], and the kicked

Harper model [66] on a QIP. Although localization can in principle be observed in an ideal emulation using as few as three qubits [6], the sensitivity of this phenomenon to noise effects [6, 7, 65–67, 84, 99] poses a rigorous challenge in the task of creating and maintaining a localized state on a noisy QIP.

In our experiment, we explored localization on a small (3-qubit) QIP based on liquid state NMR [48]. The aim of the study was to implement the sawtooth map on our QIP, to do so in such a way that we observe properties of localization which are clearly distinct from the classical behavior, and to use this example emulation as a test of the precision of our implementation as well as to motivate the continued refinement of this implementation.

Since liquid state NMR QIP relies on a large spatially distributed ensemble of quantum systems, we have to be careful in selecting the measures that we use for observing localization. The errors in our implementation of the sawtooth map will vary over the ensemble due to the inhomogeneity of the rf control field. There will be regions of the ensemble where the fidelity of implementation of the sawtooth map is sufficient that we observe localization, while for other regions the errors will be large enough to prevent localization. In the experiment we observe the sum of these effects, and thus we expect to see a peak in the probability distribution in the basis of localization that is representative of those parts of the ensemble that are localized, accompanied by a background offset in the probability distribution in the basis of localization resulting from those parts of the ensemble that are not localized.

A description of the sawtooth map is given in Sec. 2.1, followed by an explanation of the experimental implementation of the map in Sec. 2.2. A discussion of the noise effects expected in the experiment are presented in Sec. 2.3, along with a discussion of their effects on the localization phenomenon. In Sec. 2.4 the experimental results are reported and shown to demonstrate properties which are consistent with localization. The results are further compared with numerical simulations of the experiment which show that the imperfections in the data are well accounted for by the error model identified in previous work [10, 88, 115]. Finally, in Sec. 2.5, numerical studies of the error model are applied to measure the relative degree of delocalization caused by the specific noise mechanisms.

## 2.1 The sawtooth map

The sawtooth map is a periodically kicked system with period  $T$  and kick strength  $k$ , whose classical dynamics are dictated by a single parameter  $K = kT$ . One iteration of the classical sawtooth map is compactly described by the equations

$$\begin{aligned}\bar{J} &= J + k(\Theta - \pi) \\ \bar{\Theta} &= \Theta + T\bar{J}\end{aligned}\tag{2.1}$$

where  $\Theta$  is the angular position variable and  $J$  is the angular momentum variable. The cylindrical phase space, which results from the periodicity of the position variable ( $0 \leq \Theta < 2\pi$ ), can be represented on a torus by truncating the momentum space to length  $2\pi L/T$  and applying a periodic boundary condition. In the quantum regime, one iteration of the sawtooth map is represented by the unitary time evolution operator

$$U_{saw}(0, T) = \exp\left(-iT\hat{J}^2/2\right) \exp\left(ik(\hat{\Theta} - \pi)^2/2\right)\tag{2.2}$$

where  $\hat{J}$  and  $\hat{\Theta}$  are conjugate action quantum mechanical operators. The state of the quantum system is represented by a density matrix  $\hat{\rho}$  expressed in the momentum basis. A detailed description and insightful discussion of the sawtooth map can be found in reference [6].

In a simulation of the quantum sawtooth map on an  $n_q$  qubit quantum information processor, the momentum basis states of the emulated system are represented by  $N = 2^{n_q}$  computational basis states, therefore  $N = 2\pi L/T$ . The momentum basis states are labeled by their eigenvalues  $-N/2 \leq j < N/2$ , such that  $\hat{J}|j\rangle = j|j\rangle$ . The position basis states  $|\theta_m\rangle$  have eigenvalues  $\theta_m = (2\pi m/N)$ , such that  $\hat{\Theta}|\theta_m\rangle = \theta_m|\theta_m\rangle$ , where  $0 \leq m < N$ . The overlap between conjugate basis states is given by

$$\langle\theta_m|j\rangle = \frac{1}{\sqrt{N}} \exp\left[\frac{2\pi im}{N} \left(j + \frac{N}{2}\right)\right]\tag{2.3}$$

**Quantum localization.** In the classical phase space, when  $K < -4$  or  $K > 0$ , the sawtooth map induces chaotic motion, which is seen by considering a classical ensemble of trajectories, where each element of the ensemble has a fixed initial momentum ( $J = 0$ ) and

a randomized initial position ( $\Theta$ ). The chaotic motion arises due to the presence of the term  $k(\Theta - \pi)$  in Eq. 2.1, which gives a *kick* to the momentum at each iteration of the map. In chaotic parameter regimes, the strength of the sequence of kicks can be approximated as a quasi-random sequence, leading to diffusive broadening along the momentum dimension of the classical phase space, as shown in Fig. 2-1. As a result, the breadth of the distribution, as measured by its second moment, grows linearly with the number of map iterations,  $n$ , according to

$$\langle(\Delta J)^2\rangle \approx Dn, \quad (2.4)$$

where  $D \approx (\pi^2/3)k^2$  is the classical diffusion coefficient. As the map is iterated, momentum diffusion continues indefinitely, and the probability distribution approaches uniformity over the bounded toroidal phase space.

The quantum system demonstrates a strikingly different behavior. Like the classical map, the quantum sawtooth map initially causes diffusive broadening in the momentum basis according to the classical diffusion coefficient  $D$ . However, after  $n^* \approx D$  iterations of the quantum map, diffusion is suppressed due to quantum interference, and for all subsequent iterations, the quantum state maintains roughly the same exponentially localized profile over the momentum basis. This surprising interference effect requires the coherence of the quantum state. The square root of the quantum standard deviation  $\sqrt{\langle(\Delta \hat{J})^2\rangle}$  represents the number of states that are significantly populated in the system, and is essentially static after  $n^*$  iterations, representing the onset of localization. Therefore, the localization length

$$l = \sqrt{\langle(\Delta \hat{J})^2\rangle} = \sqrt{Dn^*} \quad (2.5)$$

serves as a useful parameter for characterizing a localized state. The inverse participation ratio (IPR) is another useful quantity for describing localized states [7]. However, the IPR of a localized state is approximately half of the localization length, and the IPR has a minimum value of 1. Therefore the IPR is not useful in the parameter regime discussed here, where  $l < 2$ .

The heuristic approximation  $n^* \approx D \approx l$  [8] yields a theoretical prediction of the localization length based on the kick strength  $l \approx (\pi^2/3)k^2$ . Quantum localization occurs when the localization length is less than the total breadth of the phase space  $N$ . However, the degree to which a physical system becomes localized may be reduced by noise effects,



as this unique quantum phenomenon is quite sensitive to decoherence and other types of errors [65, 67, 84, 99]. This sensitivity poses a rigorous challenge when trying to create and maintain a localized state on a noisy QIP.

The implementation of the quantum sawtooth map reported here takes  $L = 7$ ,  $K = 1.5$ ,  $N = 8$ , which corresponds to the classically chaotic regime, with a diffusion coefficient of  $D \approx (\pi^2/3)k^2 = 0.24$ . The theoretical approximation that  $n^* \approx D$  predicts that the system will be localized after one iteration of the map ( $n^* < 1$ ). This effect is known as perturbative localization, where the system is localized without the initial diffusive behavior. The results of numerical simulations plotted in Fig. 2-1 confirm this prediction, as the breadth of the probability distribution is essentially static after a single iteration of the quantum map.

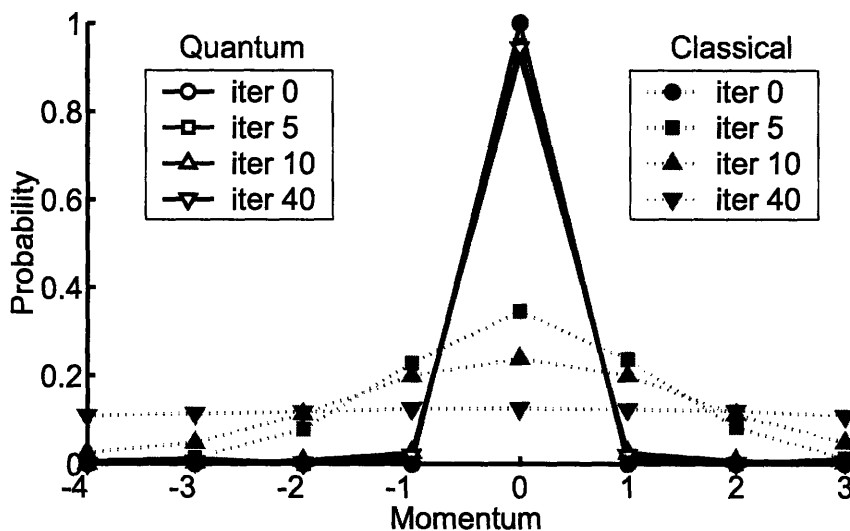


Figure 2-1: The momentum distribution after 0, 5, 10, and 40 iterations of the classical (red, filled markers) and quantum (blue, unfilled markers) sawtooth maps ( $L = 7$ ,  $K = 1.5$ ,  $N = 8$ ). The classical distribution represents 20,000 realizations of the map, with initial momenta  $j = 0$  and random initial positions uniformly distributed over the phase space. The initial quantum state is the  $j = 0$  momentum eigenstate. In the quantum case, the momentum is discrete, and each data point represents the population of the indicated momentum state. In the classical case, the momentum is continuous, and each data point represents the probability of momentum being in the range of the indicated value  $\pm 1/2$ . The classical map is chaotic, which leads to the observed diffusive broadening. In the quantum map, since the localization length is less than 1, the state remains exponentially localized after a single iteration. The breadth of the momentum distribution is essentially static in the quantum case, and only the  $j = 0$  momentum state is significantly populated.

## 2.2 Implementation details

An algorithm for the quantum sawtooth map can be generated by expressing the matrix elements of the map in the momentum basis:

$$\begin{aligned}
\langle j | U_{saw} | j' \rangle &= \sum_m \langle j | \exp(-iT\hat{J}^2/2) | \theta_m \rangle \langle \theta_m | \exp(ik(\hat{\Theta} - \pi)^2/2) | j' \rangle \\
&= \sum_m \exp(-iTj^2/2) \langle j | \theta_m \rangle \exp(ik(\theta_m - \pi)^2/2) \langle \theta_m | j' \rangle \\
&= \langle J | U_J U_{QFT}^{-1} U_\Theta U_{QFT} | j' \rangle
\end{aligned} \tag{2.6}$$

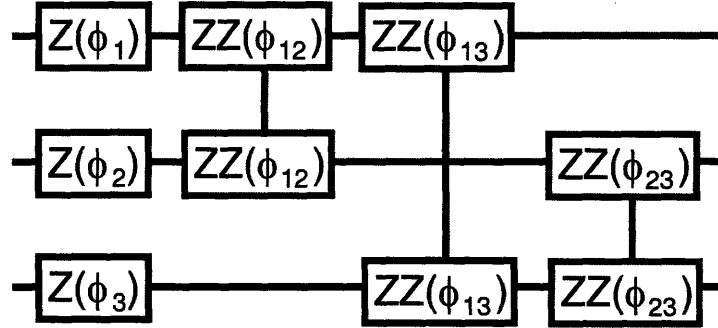
where  $U_{QFT}$  is the familiar Quantum Fourier Transform (QFT) which has the action of toggling between the position and momentum basis representations, and the diagonal free evolution and kick operators,  $U_J$  and  $U_\Theta$ , are defined

$$\langle j | U_J | j' \rangle = \exp(-iTj^2/2) \langle j | j' \rangle \tag{2.7}$$

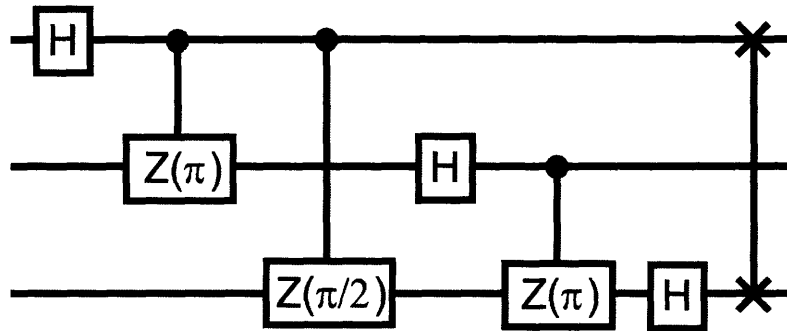
$$\langle \theta_m | U_\Theta | \theta'_m \rangle = \exp(ik(\theta_m - \pi)^2/2) \langle \theta_m | \theta'_m \rangle. \tag{2.8}$$

This form of the quantum sawtooth map ( $U_{saw} = U_J U_{QFT}^{-1} U_\Theta U_{QFT}$ ) reveals the underlying structure of the map: After the system is initialized to a momentum basis state, the first operation in the quantum sawtooth map, the QFT, transforms the system to the position basis representation, where the diagonal kick operator  $U_\Theta$  applies an impulse force. The inverse of the QFT is applied next, returning the system to the momentum basis representation, where the diagonal free evolution operator  $U_J$  is applied. These four steps ( $U_{QFT}, U_\Theta, U_{QFT}^{-1}, U_J$ ) constitute a single iteration of the quantum sawtooth map. After iterating the map, the localized probability distribution corresponds to the diagonal elements of the density matrix,  $W_j \equiv \langle j | \hat{\rho} | j \rangle$ . Realizing that the only effect of the free evolution operator is to apply a phase to the coefficient of each momentum basis state,  $U_J$  can be neglected in the final iteration of the map, since a phase does not alter the measured probabilities in that basis.

**Quantum circuits.** A quantum circuit for the QFT is derived in [82] and shown in Fig. 2-2(b). Prior implementations and experimental analysis of the QFT are described in [115, 117]. Circuits for  $U_J$  and  $U_\Theta$  are conveniently found in realizing that any diagonal



(a) Diagonal operator circuit



(b) Quantum Fourier Transform (QFT) circuit

Figure 2-2: Quantum circuits for implementing the quantum sawtooth map. For both circuits,  $Z(\chi)$  on qubit  $l$  indicates the  $Z$ -rotation,  $\exp(-i\chi\sigma_z^l/2)$ .  $ZZ(\chi)$  on qubits  $l$  and  $k$  indicates the two-qubit operation  $\exp(-i\chi\sigma_z^l\sigma_z^k)$ .  $H$  indicates the Hadamard operator  $(\sigma_x^l + \sigma_z^l)/\sqrt{2}$ , and the two-qubit operation at the end of the QFT is the swap gate. (Top) The circuit for implementing any diagonal unitary operator. This circuit can be parameterized for either the diagonal free evolution operator  $U_J$  or the diagonal kick operator  $U_\Theta$  using  $\phi_l = 2^{l-1}(\alpha + 7\beta)$  and  $\phi_{lk} = 2^{l+k-3}\beta$ , where the  $\alpha_J$ ,  $\alpha_\Theta$ ,  $\beta_J$  and  $\beta_\Theta$  derived in the text. (Bottom) The QFT and its inverse are both used to implement the quantum sawtooth map.

operator can be decomposed into a series of single-qubit Z-rotations and two-qubit ZZ-interactions. The quantum sawtooth map is emulated by programming the gates in Fig. 2-2(a) to implement  $U_J$  and  $U_\Theta$ . Parameterization of the circuit follows from a decomposition of the basis number operator  $\hat{M}|m\rangle = m|m\rangle$ , where  $0 \leq m < N$ , into a sum of products of spin operators

$$\hat{M}|m\rangle = \sum_{l=1}^{n_q} (\mathbb{1} - \sigma_z^l) 2^{l-2} |m\rangle, \quad (2.9)$$

where  $\sigma_z^l$  indicates the Pauli operator  $\sigma_z$  acting on the  $l^{\text{th}}$  qubit. For example  $\sigma_z^{(l=n_q)} = \sigma_z \otimes 1 \otimes \cdots \otimes 1$ , and  $\hat{M}|10 \cdots 0\rangle = 2^{n_q} |10 \cdots 0\rangle$ .

In general,

$$\exp(-i\alpha\hat{M}) = \exp\left(-i\alpha \sum_{l=1}^{n_q} (\mathbb{1} - \sigma_z^l) 2^{l-1}\right) \quad (2.10)$$

$$\propto \exp\left(+i\alpha \sum_{l=1}^{n_q} \sigma_z^l 2^{l-1}\right) \quad (2.11)$$

$$\begin{aligned} \exp(-i\beta\hat{M}^2) &\propto \exp\left(+i\beta \left(\sum_{j=1}^{n_q} 2^{j-1}\right) \sum_{l=1}^{n_q} \sigma_z^l 2^{l-2}\right) \cdots \\ &\exp\left(-i\beta \sum_{l < j}^{n_q} 2^{l+j-3} \sigma_z^l \sigma_z^j\right) \end{aligned} \quad (2.12)$$

where  $\propto$  indicates terms proportional to identity have been dropped since they have no observable effect on the quantum state. By identifying  $\hat{\Theta} = 2\pi\hat{M}/N$ , we can write the diagonal kick operator

$$U_\Theta = \exp\left(ik(\hat{\Theta} - \pi)^2/2\right) = \exp\left(\frac{ik}{2} \left(\frac{2\pi\hat{M}}{N} - \pi\right)^2\right) \quad (2.13)$$

$$\propto \exp\left(\frac{+i2k\pi^2}{N^2} (\hat{M}^2 - N\hat{M})\right) \quad (2.14)$$

$$\begin{aligned} &\propto \exp\left(+i \left(\alpha_\theta + \left(\sum_{j=1}^{n_q} 2^{j-1}\right) \beta_\theta\right) \sum_{l=1}^{n_q} \sigma_z^l 2^{l-1}\right) \cdots \\ &\exp\left(-i\beta_\theta \sum_{l < j}^{n_q} 2^{l+j-3} \sigma_z^l \sigma_z^j\right) \end{aligned} \quad (2.15)$$

where we have defined

$$\alpha_\theta \equiv 2k\pi^2/N \quad (2.16)$$

$$\beta_\theta \equiv -2k\pi^2/N^2. \quad (2.17)$$

Equation 2.15 indicates that  $U_\Theta$  is implemented by  $n_q$  single-qubit  $Z$ -rotations and  $3n^2$  two-qubit  $ZZ$ -interactions. Each operation is parameterized by the values in the exponents of equation 2.15.

The parameters for implementing the diagonal free evolution operator can be found in a similar manner by recognizing that  $\hat{J} = \hat{M} - N/2$ , and therefore

$$U_J = \exp\left(-iT\hat{J}^2/2\right) = \exp\left(\frac{-iT}{2}\left(\hat{M} - \frac{N}{2}\right)^2\right) \quad (2.18)$$

$$\propto \exp\left(\frac{-iT}{2}\left(\hat{M}^2 - N\hat{M}\right)\right) \quad (2.19)$$

$$\begin{aligned} &\propto \exp\left(+i\left(\alpha_J + \left(\sum_{j=1}^{n_q} 2^{j-1}\right)\beta_J\right)\sum_{l=1}^{n_q}\sigma_z^l 2^{l-2}\right)\dots \\ &\exp\left(-i\beta_J\sum_{l<j}^{n_q} 2^{l+j-3}\sigma_z^l\sigma_z^j\right) \end{aligned} \quad (2.20)$$

where we have defined

$$\alpha_J \equiv -TN/2 \equiv -\pi L \quad (2.21)$$

$$\beta_J \equiv T. \quad (2.22)$$

This circuit for the quantum sawtooth map is computationally efficient, in that the number of fundamental quantum gates required to implement the algorithm depends polynomially on the number of qubits [7].

**NMR QIPs.** In NMR quantum information processing, nuclear spins polarized by a strong external magnetic field serve as qubits. The molecule used in this experiment, diagrammed in Fig. 2-3, is tris(trimethylsilyl)silane-acetylene dissolved in deuterated chloroform. The carbon nuclei in the acetylene branch are carbon-13 enriched, and the methyl carbons are of natural isotopic abundance. The two carbon-13 nuclei and the hydrogen nucleus in the acetylene branch are used as qubits. The full internal Hamiltonian has the

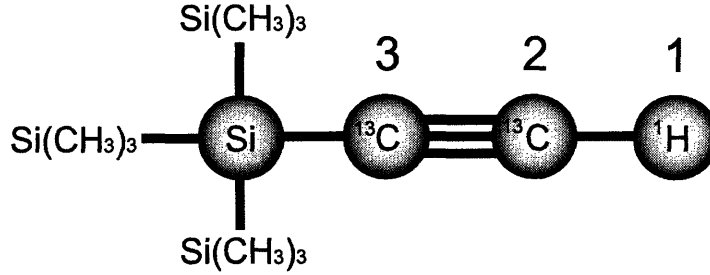


Figure 2-3: A diagram of the tris(trimethylsilyl)silane-acetylene molecule used to simulate the quantum sawtooth map in a liquid state NMR QIP. The hydrogen nucleus in the acetylene branch is labeled qubit 1 in the experiment; the two carbon-13 nuclei in the acetylene branch are labeled qubits 2 and 3.

form

$$\mathcal{H}_{int} = \sum_{i=1}^{n_q} \pi \nu_i \sigma_z^i + \sum_{j < k} \frac{\pi J_{jk}}{2} \sigma^j \cdot \sigma^k \quad (2.23)$$

where  $\nu_i$  is the resonance frequency of the  $i^{th}$  spin, and  $J_{jk}$  is the frequency of scalar coupling between spins  $j$  and  $k$ . Note that  $J_{jk}$  is not related to the quantum operator  $\hat{J}$ . The hydrogen nucleus is labeled qubit number 1, making it the most significant bit in the computational state vector. The carbon qubits are labeled as indicated in Fig. 2-3. Experiments are performed in a 9.4 Tesla magnetic field, where the Carbon qubits are separated by 1.201 kHz. The scalar couplings are  $J_{12} = 235.7$  Hz,  $J_{23} = 132.6$  Hz, and  $J_{13} = 42.9$  Hz. Because the spin system is in a highly mixed state at room temperature, the system was prepared in a pseudopure state [20] by the technique described in [104]. Three readout sequences were needed to measure the eight diagonal elements of the density matrix, which correspond to the distribution of momentum basis states.

**Pulse sequences.** The average gate fidelity [37] of each unitary control sequence was optimized over the full Hilbert space. The input state preparation pulse sequence, which is non-unitary, was optimized based on the state correlation [37] between the simulated input state  $\hat{\rho}_{sim}$  and the ideal input state  $\hat{\rho}_{ideal} = |100\rangle\langle 100|$ . The average fidelity (or state correlation) of each implemented pulse sequence, as calculated by numerical simulation, is listed in Table 2.1. The NMR pulse sequence for one full iteration of the quantum sawtooth map is shown in Fig. 2-4.

Table 2.1: Pulse sequences designed for the quantum sawtooth map experiment. Fidelities are calculated by numerical simulations which account for rf inhomogeneity, neglecting decoherence effects.

Map	Duration (ms)	Fidelity
Input State Preparation	50	$Corr = 0.99$
QFT	6	0.99
QFT Inverse	6	0.99
$J$ Diagonal	50	0.99
$\Theta$ Diagonal	20	0.99
Readout 1	0.01	1.00
Readout 2	62	0.98
Readout 3	72	0.98

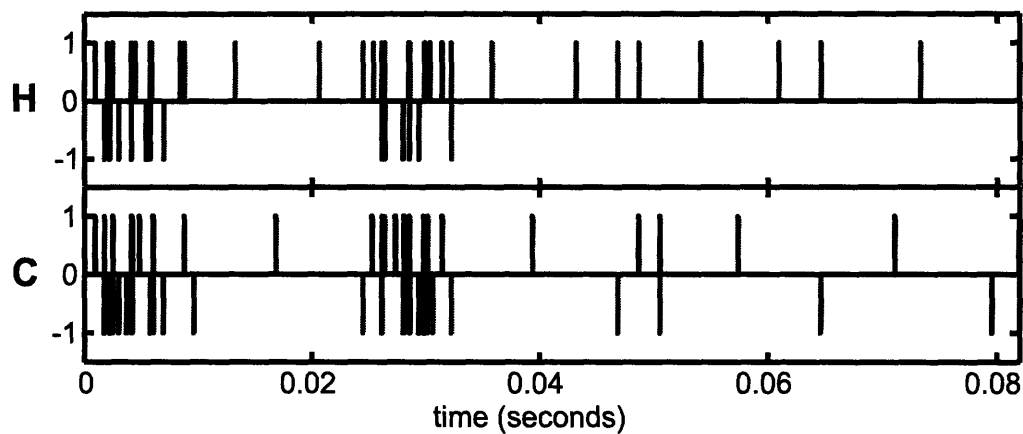


Figure 2-4: The hydrogen (H) and carbon (C) rf control fields versus time for the full quantum sawtooth map pulse sequence. Red versus blue pulses are 90 degrees out of phase; pulses above versus below the horizontal axis are 180 degrees out of phase. The nutation frequency of each hydrogen (carbon) pulse is 46.7 kHz (17.5 kHz).

## 2.3 Numerical simulation

Through numerical simulation of the experiment, it is possible to predict the behavior of the system under the optimized control sequence in the presence of various types of noise known to influence the QIP. Errors affecting the implementation of the quantum sawtooth map are conveniently classified in three categories [10, 88, 115] - coherent errors, decoherent errors, and incoherent errors - which can be generally used to categorize the errors affecting any QIP. Each type of error delocalizes the system in a different manner.

In the presence of coherent errors, the system evolves under a unitary process other than the ideal quantum sawtooth map. Due to their unitary nature, coherent errors are reversible. The coherent errors modeled in numerical simulations arise in the experiment due to strong coupling between the carbon qubits, as well as the action of the internal Hamiltonian during rf pulses. Coherent errors delocalize the system by introducing unitary transitions between momentum states.

Decoherent errors cause the individual members of the ensemble (and hence the observed ensemble average) to evolve in a non-unitary fashion. Decoherent evolution can be modeled as a coupling between the system and an external environment and can usually be represented by a completely positive linear map, expressed as an  $N^2 \times N^2$  superoperator  $\hat{S}$  acting on a columnized  $N^2 \times 1$  state vector  $|\rho\rangle$ , according to

$$|\rho_{out}\rangle = \hat{S} |\rho_{in}\rangle. \quad (2.24)$$

Decoherent errors are accounted for in numerical simulations by allowing the system to evolve under an approximate relaxation superoperator [35], which is completely diagonal in the generalized Pauli basis. In this diagonal form, each non-zero entry in the relaxation superoperator represents the decoherence rate of a generalized Pauli basis operator; the specific values used in simulations are based on measurements of all T1s in the three qubit system as well as the single species T2s.

Given the time scale of one full iteration of the quantum sawtooth map ( $10^{-1}$ s) compared to the system's typical decoherence rates ( $1 \text{ s}^{-1}$ ), decoherence in this system is in the moderately dissipative regime, which has been shown to cause delocalization in the quantum sawtooth map [65]. The non-unitary, dissipative action of decoherence along with the mixing action of the control sequence causes an essentially uniform damping of the



measured probability distribution, accompanied by a uniform background offset that conserves probability. The background offset in probability appears in the density matrix as an increased identity component, which represents a loss of system purity and a corresponding increase in the von Neumann entropy of the system. In this way, the effect of decoherence is to mimic the diffusive, chaotic dynamics of the classical system described in Sec. 2.1.

Incoherent errors occur when the various members of the experimental ensemble experience a distribution of unitary time evolution operators. Incoherent evolution can be generally expressed as an operator sum

$$\rho_{out}^{inc} = \sum_k p(k) U_k \rho_{in} U_k^\dagger, \quad (2.25)$$

where  $p(k)$  is the probability that a member of the ensemble will undergo unitary time evolution under  $U_k$ . Under incoherent errors, the individual members of the ensemble evolve coherently, but the ensemble-averaged time evolution of the system is non-unitary. The dominant incoherent errors in the experiment arise due to the inhomogeneity of the rf field over the spatial extent of the liquid state NMR sample. When an rf pulse is applied during the experiment, the members of the ensemble experience a distribution of rf powers, and only a fraction of the ensemble actually experiences precisely the nominal (ideal) rf power. In numerical simulations, we can approximate the effects of the continuous distribution of carbon rf powers by simulating a previously measured distribution of nine discrete bins of rf power, plotted in Fig. 2-5. Bin 6 represents the largest portion of the ensemble and corresponds to the nominal rf power, while the other eight bins result from the inhomogeneity of the rf control field. In the experiment, there are two dimensions of incoherence: one for both the proton and carbon rf-control fields. In numerical simulations presented in Sections 2.4 and 2.5, the continuous distribution of carbon and hydrogen rf power correlations is approximated by a discrete two-dimensional ( $9 \times 9$ ) rf probability distribution function.

Simulating only the one-dimensional distribution of carbon rf power in Fig. 2-5 is sufficient for gaining a qualitative understanding of the effects of incoherent noise in the experiment. Figure 2-6 shows the results of numerical simulations of the experimentally implemented control sequence for each bin of rf power; the simulations include decoherence effects. Due to the incoherence, the local errors are different for each bin. Consequently, in regions of the ensemble where the rf power is near the nominal rf power (see Bins 6

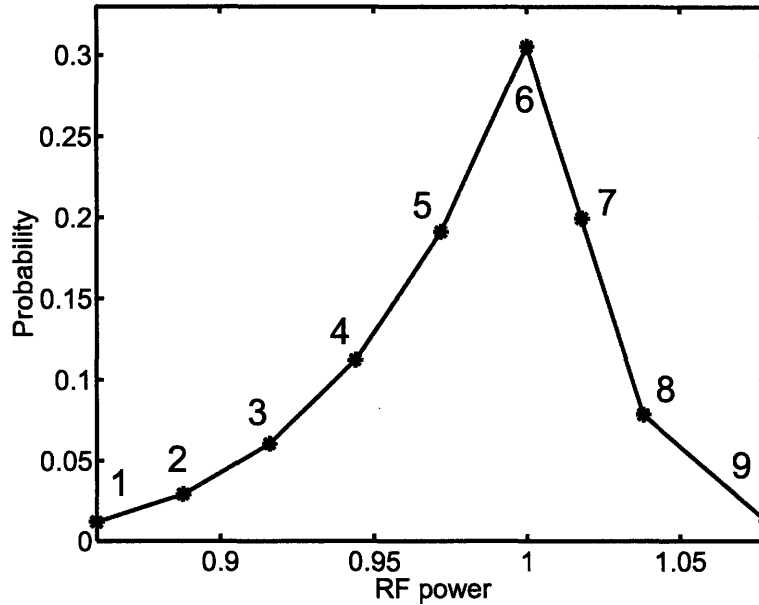


Figure 2-5: The nine point distribution of carbon rf powers measured in previous experiments and used to simulate the experimentally implemented control sequence for the quantum sawtooth map. The carbon rf power is in units of the nominal carbon nutation frequency, 17.5 kHz. The numerals labeling each point in the distribution indicate the associated bin of incoherence in Fig 2-6.

through 8), the fidelity of implementation of the sawtooth map is sufficient that we observe localization. For other regions which constitute a smaller percentage of the ensemble (e.g. Bin 1), the errors are large enough to prevent localization and the momentum distribution is broad. Hence we see that in the experiment, when we observe the weighted average of these distributions, the (more abundant) localized portions of the ensemble will appear as a peak in the  $j = 0$  momentum state, and the delocalized portions of the ensemble will contribute an approximately uniform background offset across the momentum distribution.

Another important insight gained from analyzing distributions plotted in Fig. 2-6 is that the bins where the rf power is near ideal are relatively unaffected by decoherence. Consequently, we expect incoherence rather than decoherence to be the principle source of noise compromising our ability to observe localization over the ensemble. This is discussed in more depth in Sec. 2.5.

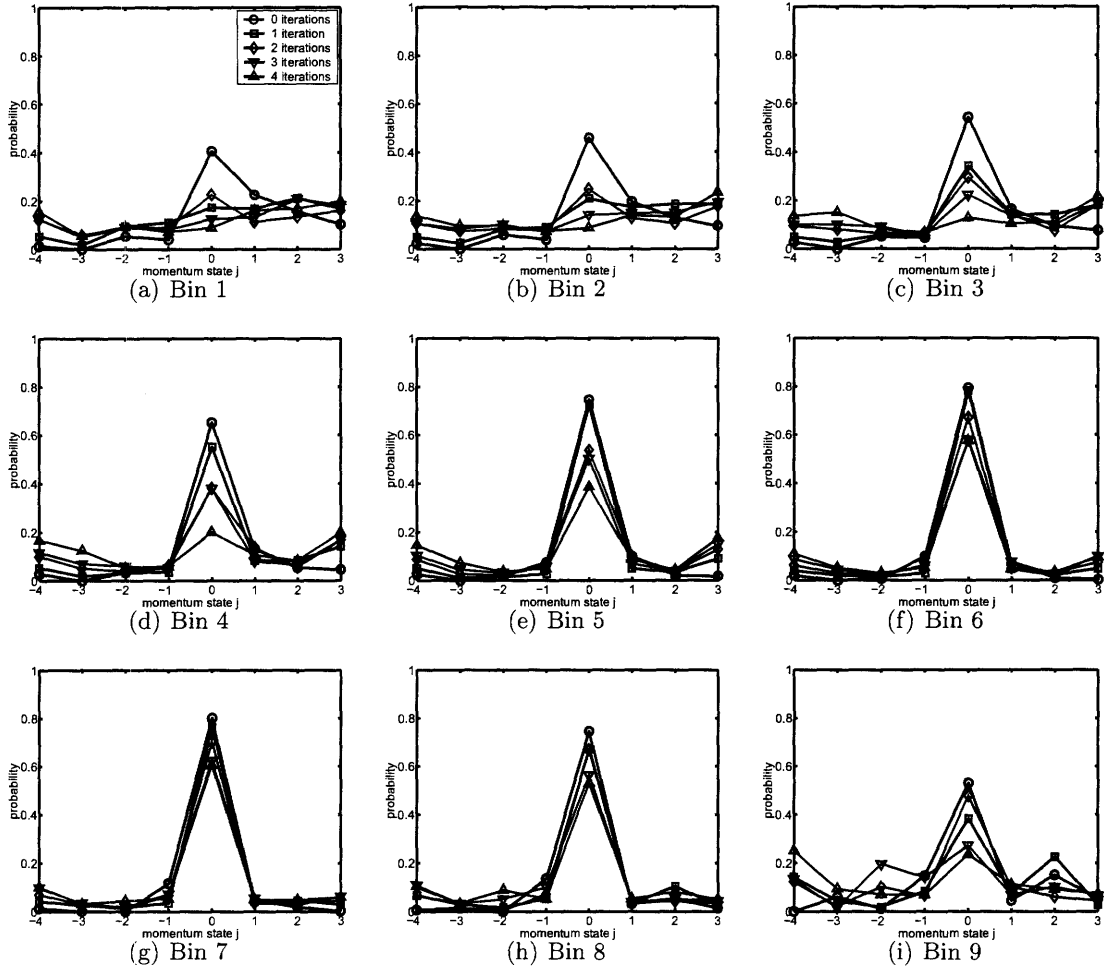


Figure 2-6: Momentum profiles for different regions of the ensemble generated by numerical simulations of the experiment which account for T1 and T2 decoherence. Each plot represents the momentum profile resulting from a numerical simulation of the control sequence (zero through four iterations) with the carbon rf power indicated in Fig. 2-5. Bin 6 represents the nominal rf power, which has the highest fidelity when compared to the ideal quantum sawtooth map. The distributions simulated near the nominal rf power appear to be localized, while those far from the nominal rf power are quickly delocalized. In experiments, the average over the incoherence is observed (weighted by the probability distribution in Fig. 2-5).

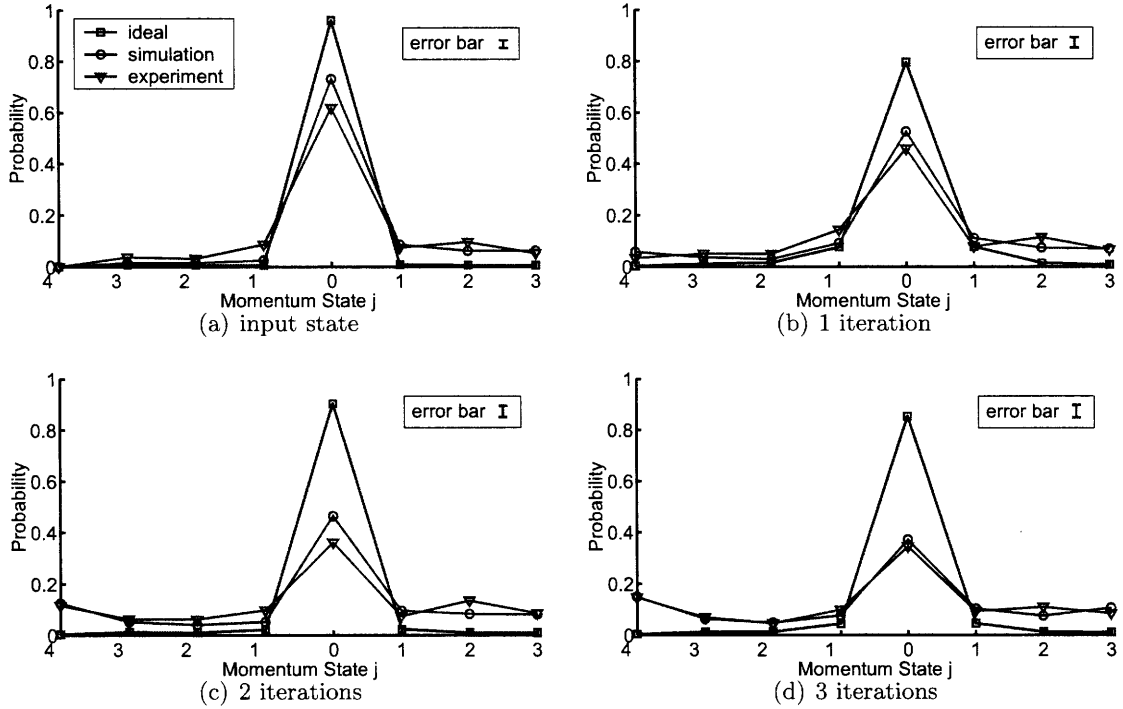


Figure 2-7: The momentum distribution after 0 through 3 iterations of the quantum sawtooth map ( $L = 7$ ,  $K = 1.5$ ,  $N = 8$ ) for the experiment (triangles), a numerical simulation of the experiment which is not affected by noise (squares), and finally a numerical simulation of the experiment which includes coherent errors, decoherence effects, and incoherent errors due to rf inhomogeneity in both the carbon and hydrogen control fields (circles). Error bars are drawn to scale for each iteration. The population of the initial state ( $j = 0$ ) dominates the distribution through 3 iterations of the experiment, and the width of the central peak is essentially unchanged. However, experimental noise clearly causes the ensemble-averaged state to delocalize through the appearance of a baseline offset over the momentum distribution.

## 2.4 Experimental results

In Fig. 2-7, the experimentally measured probability distributions after zero through three iterations of the quantum sawtooth map are plotted along with the ideal distributions and the distributions obtained by numerical simulations of the experiment which account for decoherence and the full two-dimensional distribution of rf powers. The experimental data reveals that the interior region of the momentum distribution does not broaden, as in a diffusive regime, but rather, the peak maintains roughly the same breadth, as predicted by simulations. Meanwhile, the increasing background probability offset reveals the presence of imperfections in the implemented map, representing those regions of the ensemble which

are not localized due to incoherence. These qualitative features of the experimental data are reflected in the quantitative measures of localization discussed later.

Discrepancies between the ideal and experimentally observed behavior are caused by experimental noise and decoherence influencing the implementation of quantum sawtooth map, in addition to imperfections in the experimentally prepared input state and in the readout steps. Figure 2-7 reveals, on a qualitative level, that these discrepancies are well accounted for by the noise model used in numerical simulations. The relative contribution of the distinct noise mechanisms to the experimentally observed delocalization of the state is discussed further Sec. 2.5.

In light of the incoherent variations of localization properties of the map over the ensemble, we wish to select a measure that can be interpreted as the extent to which some portion of the ensemble demonstrates quantum localization. By measuring the full width at half maximum (FWHM) of the probability distribution in successive iterations, we can observe the presence of any dynamical broadening of the distribution, without regard to the background probability offset caused by incoherence, as discussed in Sec. 2.3. Fig. 2-8 shows a plot of the FWHM for each probability distribution plotted in Fig. 2-7. The FWHM data reveals the dynamical properties of the experimentally measured distribution as distinct from the classical behavior. The relative flatness of the experimentally measured FWHM curve through three iterations of the map is consistent with quantum localization in an incoherent ensemble. Numerical simulations show the progression in peak width from the ideal simulation (most narrow) to simulations where decoherence and incoherence are included in the simulation. The numerical simulation which accounts for decoherence but not incoherence corresponds to the momentum distributions plotted in Bin 6 of Fig. 2-6.

## 2.5 Discussion

By using numerical simulations to isolate the various types of errors known to influence the experiment, it is possible to measure the relative significance of each type of error by examining the degree to which it leads to delocalization in the system. Figure 2-9 shows the degree to which each type of error causes delocalization in the resulting state, as measured by the second moment of the corresponding probability distribution, thus distinguishing the relative importance of the distinct noise mechanisms in the experiment. The data also

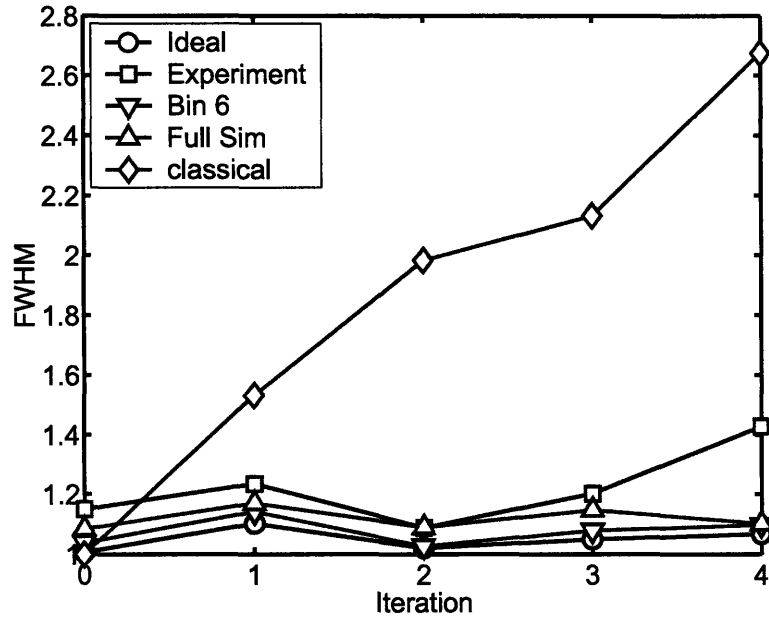


Figure 2-8: The full width at half maximum of the momentum distribution after zero through four iterations of the sawtooth map in various implementations: a numerical simulation of the exact classical map (diamonds), a numerical simulation of the exact quantum map (circles), the experimentally implemented map (squares), a numerical simulation of the experimentally implemented map which accounts for decoherence without incoherence (triangles down), a numerical simulation of the experimentally implemented map which accounts for decoherence with incoherence (triangles up). The FWHM reveals that despite the noise affecting the QIP, the distribution mimics the ideal quantum behavior, and does not broaden in a diffusive manner as in the classical case.

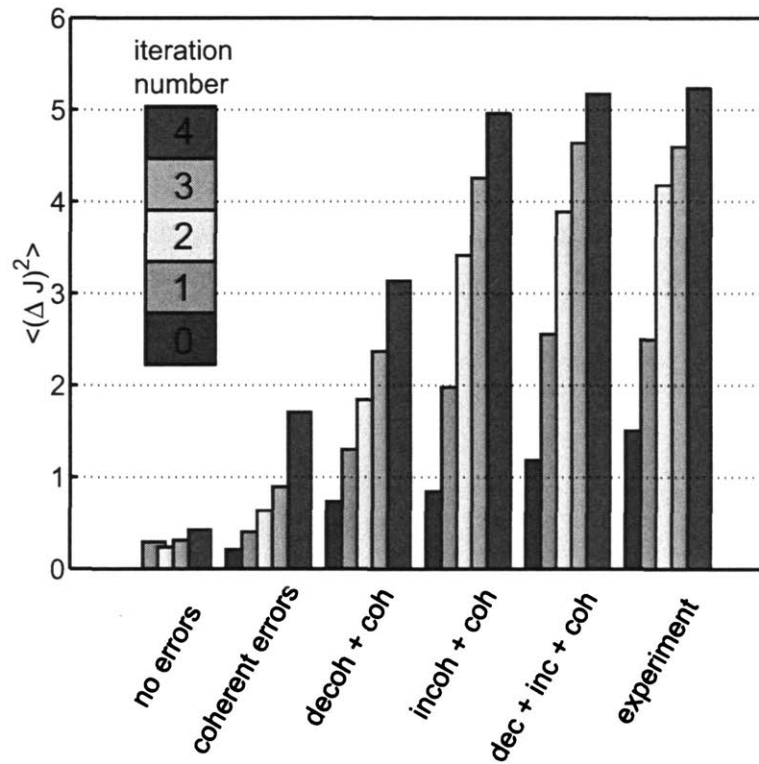


Figure 2-9: The second moment of the probability distribution determined from numerical simulations of the experiment including the error models discussed in the text, compared to the ideal data and the experimental data. This plot demonstrates the relative importance of the individual noise mechanisms as they contribute to the experimentally observed delocalization process. As more errors are included in numerical simulations, the system shows stronger delocalization and more closely emulates the experimental data.

reveals the extent to which the breadth of the distribution is affected by errors in the initial state preparation. Evidently, the coherent errors are essentially inconsequential over at least three iterations of the map. The slope of second moment versus time plot is most strongly affected by incoherent errors, and thus incoherence is determined to be the dominant noise mechanism limiting the degree to which localization is achieved by experimental control, which is consistent with the observations of Sec. 2.3.

Additional insight on the delocalizing effects of experimental noise and decoherence can be gained by examining the superoperators and the corresponding Kraus operators for each type of numerical simulation. A superoperator of dimension  $N^2 \times N^2$  which describes a completely positive quantum process can be equivalently expressed as an operator sum, which involves at most  $N$  Kraus operators of dimension  $N \times N$  [60]. That is to say that for a general quantum process as in Eq. 2.24,

$$|\rho_{out}\rangle = S |\rho_{in}\rangle \quad (2.26)$$

there is an equivalent representation of the form

$$\rho_{out} = \sum_k A_k \rho_{in} A_k^\dagger \quad (2.27)$$

where  $A_k$  is the  $k^{th}$  Kraus operator, which has a magnitude of  $\|A_k\|$ . Methods for conversion to and analysis of the Kraus form are given in [47] and [115]. The Kraus form for an ideal implementation of a unitary process would consist of a single Kraus operator which is the corresponding unitary operator describing the process. Therefore, in an implementation where the errors are small, we expect the Kraus operator of largest magnitude to resemble the ideal unitary operator. The numerically simulated superoperators expressed in the momentum basis, along with the largest magnitude Kraus operators, plotted in Fig. 2-10, give a qualitative picture of the differences between a quantum process that leads to localization (in the ideal simulations) and a quantum process that causes some degree of delocalization (in the simulations which include errors). Off-diagonal elements in the unitary or Kraus operator cause transitions between momentum states; diagonal elements alter the magnitude and phase of each momentum state without causing transitions. The qualitative result of the simulated noise is to reduce the bandedness (i.e. the relative magnitude of the



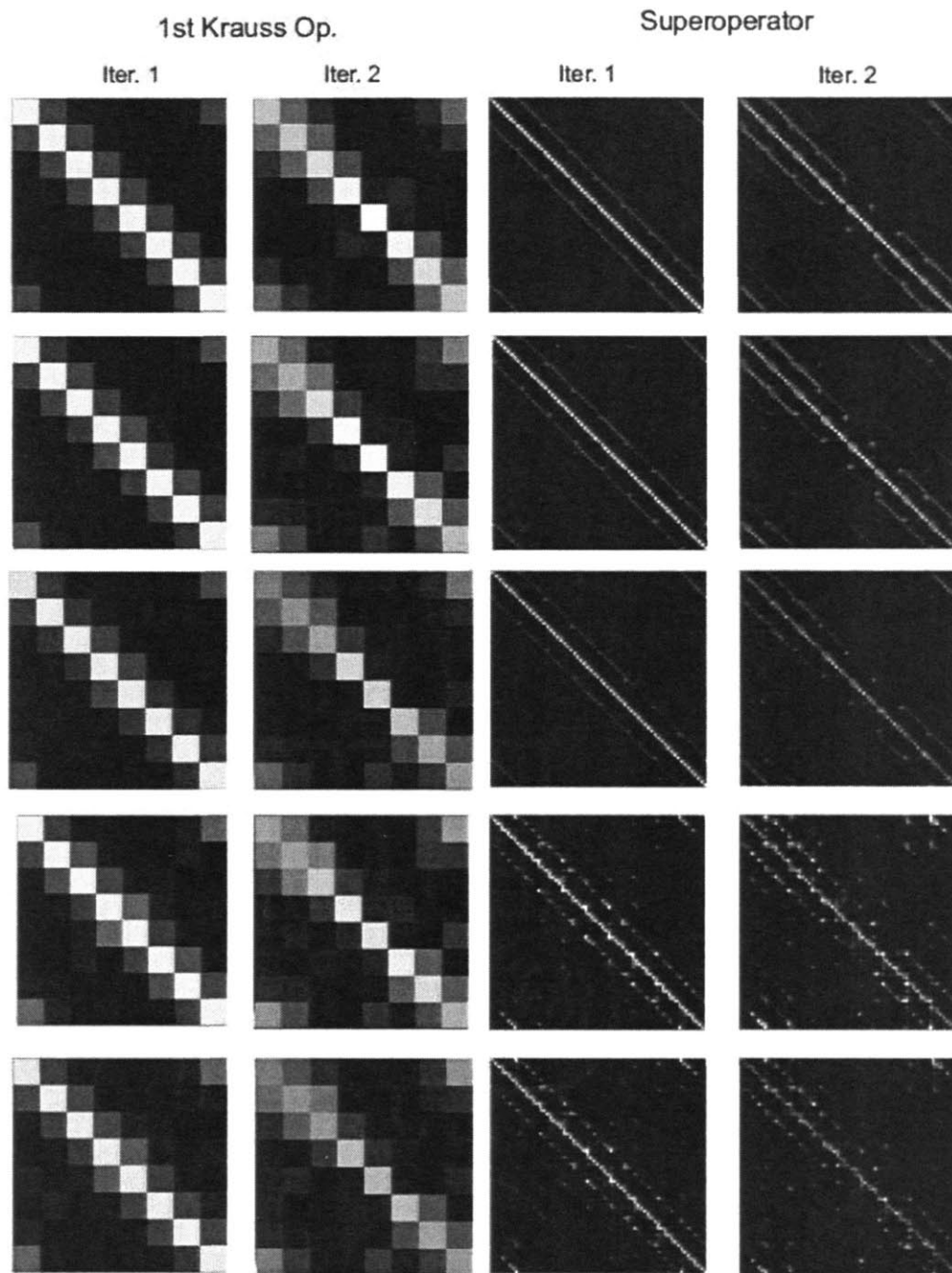


Figure 2-10: The magnitude of each element of the superoperators and most significant Kraus operators for numerical simulations of the quantum sawtooth map experiment which include different types of errors (top to bottom): (1) no errors, (2) coherent errors, (3) coherent errors and decoherent errors due to relaxation, (4) coherent errors and incoherent errors due to rf inhomogeneity, (5) coherent, incoherent, and decoherent errors. The elements are scaled from zero (black) to one (white). The errors in the implementation of the sawtooth map affect the bandedness of each Kraus operator (and similarly of each superoperator).

diagonal and near-diagonal elements compared to the off-diagonal elements) of the operator, thus reducing the degree to which a state is localized under the map. The simulated operators for 1 and 2 iterations are progressively less banded as more errors are included in the simulation, which further attests to the sensitivity of localization to experimental noise effects. As explained in Sec. 2.3, Fig. 2-10 again shows qualitatively that rf inhomogeneity has a greater delocalizing effect than decoherence in this implementation of the quantum sawtooth map.

## 2.6 Conclusions

The quantum sawtooth map has been emulated on a three qubit liquid state nuclear magnetic resonance quantum information processor in the perturbative localization parameter regime of the map ( $K = 1.5$ ,  $L = 7$ ,  $N = 8$ ). Observing the dynamic behavior of the width of the peak in the momentum probability distribution reveals behavior which is consistent with coherent quantum localization. Due to incoherent noise, this localized peak is superimposed with a uniform background offset over the probability distribution which represents those parts of the ensemble which are not localized due to local unitary errors which vary over the ensemble.

Numerical simulations of the experiment reveal that the decoherent noise known to act on the system is relatively inconsequential in this implementation of the map, in terms of its effect on localization when compared with incoherence. This study serves as a test of the capabilities of coherent control and serves to motivate the refinement of our implementation. Specifically, we see that incoherence is the biggest challenge in implementing localization, a highly sensitive quantum coherence-dependent phenomenon. Given the sensitivity of localization to various types and strengths of errors, the degree to which localization can be created and maintained in a QIP serves as a benchmark of practical relevance for assessing the overall degree of coherent control and for identifying which noise mechanisms most significantly reduce the degree of coherent control achieved in the device.

## Chapter 3

# Signatures of incoherence

Incoherent noise encodes quantum information into the classical degrees of freedom of an ensemble by a distribution of unitary errors. An incoherent process is tied to a time-independent or slowly varying classical probability distribution of Hamiltonians. Evolution under such a process is naturally described as an operator sum, given in superoperator notation by

$$\hat{S}(t) = \int p(z) e^{i\mathcal{H}(z)t} \otimes e^{-i\mathcal{H}(z)t} dz \quad (3.1)$$

where  $p(z)$  is the classical probability distribution of Hamiltonians  $\mathcal{H}(z)$ . A variety of tools have been developed to counteract incoherent noise in quantum information processors. Optimal control theory minimizes the errors caused by uncertainty in the system Hamiltonian [25, 85]. Dynamical decoupling and bang-bang control actively suppress incoherence by periodically refocusing part of the evolution [109, 111–113]. Strongly modulating pulses [88] and composite pulses [68] have also been used to refocus incoherent noise. Such techniques exploit the reversibility of incoherent errors and are particularly valuable since they do not require access to a larger Hilbert space, as do decoherence free subspaces [32, 70, 122], noiseless subsystems [58, 122] and other quantum error encodings [96, 100]. Decoherent noise by contrast does require the full power of quantum error-correcting codes, so distinguishing the presence of incoherence is important in choosing an error-correction scheme.

Incoherence, which is typically studied for single-qubit errors in  $SU(2)$ , causes a loss of purity in the ensemble-averaged state while preserving the purity of the individual ensemble members. Decoherence is a distinct process that irreversibly reduces the purity of

the individual ensemble members. In small Hilbert spaces, incoherence is easily detected and controlled either by time reversal of the control field or through creation of echoes. Some classic examples include the rotary echo [53, 91], the Hahn echo [46], the Carr-Purcell and CPMG echo sequences [15, 78]. In these examples, incoherent errors are completely refocused by an inverted incoherent process, and the resulting increase in purity over the ensemble causes an observable echo. Identifying and controlling incoherence is more difficult in Hilbert spaces that support entanglement and in particular, in the presence of an entangling operation. An entangling operation propagates incoherent errors to non-separable states, causing a loss of purity that is not recovered by an inverted incoherent process, so the incoherence mimics a decoherent process.

Here we present an example of incoherence influencing an entangling operation in a three-qubit liquid state NMR QIP, and we show how the incoherence appears as a distinct process from decoherence in the measurement of fidelity decay under imperfect motion reversal. Fidelity decay [86] has previously been shown to be a useful tool for efficiently characterizing errors in a QIP [33]. In the method suggested here, the task of measuring fidelity decay is simplified by studying fidelity decay under a cyclic operation, which removes the need to invert the ideal evolution and admits analysis by Average Hamiltonian Theory [44]. We show that in our experiment incoherence causes recurrences in fidelity that could not arise from a decoherent process. The signature of incoherence observed in experimental data is also analyzed by numerical simulations of the NMR experiment.

### 3.1 Identifying incoherence by fidelity decay

The fidelity between two quantum states  $\rho$  and  $\tilde{\rho}$  is defined

$$F = \langle \tilde{\rho} | \rho \rangle, \quad (3.2)$$

where  $|\rho\rangle$  is the density matrix represented as a state vector in Liouville space. Given an ideal unitary map  $\hat{S}$ , a perturbation  $\hat{P}$  and an initial state  $\rho_0$ , the fidelity decay after  $n$  iterations of imperfect motion reversal is

$$F_n = \langle \rho_0 | (\hat{S}^{-1})^n (\hat{P}\hat{S})^n | \rho_0 \rangle. \quad (3.3)$$

Here we consider the case where  $(\hat{P}\hat{S})$  is a noisy implementation of  $\hat{S}$ , and therefore implementing the ideal inverse map  $\hat{S}^{-1}$  is impractical. However, if we choose  $\hat{S}$  to be cyclic, then for some number of iterations  $n_c$ , we have  $(\hat{S}^{-1})^{n_c} = \hat{S}^{n_c} = \mathbf{1}$ . Now if we constrain the fidelity decay to be measured only after iterations that are an integer multiple of  $n_c$ , we have

$$F_n = \langle \rho_0 | (\hat{P}\hat{S})^n | \rho_0 \rangle, \quad (3.4)$$

thus simplifying the fidelity decay expression and measurement.

In our experiment, we are interested in distinguishing incoherence and decoherence in a fidelity decay. Here we derive an expression for the fidelity decay of an ensemble-averaged state evolving under these two types of noise using a simple noise model. For both types of noise, the measurement ensemble  $\mathcal{E}_z$  is parameterized by the classical variable  $z$ . For decoherent noise, the state fidelity decays exponentially before saturating at  $1/N$  where  $N$  is the Hilbert space dimension, a well-known result for decoherent noise [51]. For incoherent noise, we will show that the fidelity decay expression has two terms: one term that decreases as the map is iterated, and an additional term that may periodically increase, allowing for fidelity recurrences.

Let  $\hat{S}$  and  $\hat{P}_z$  represent unitary processes over a Hilbert space of dimension  $N$ . The ideal map  $\hat{S}$  acting  $n$  times on the initial state  $\rho_0$  returns the state  $\hat{S}^n |\rho_0\rangle = |\rho_n\rangle$ , while the perturbed map returns the state  $(\hat{P}_z \hat{S})^n |\rho_0\rangle = |\tilde{\rho}_n\rangle$ .  $\hat{P}_z$  is a perturbation of the form  $\exp(-i\eta_z \hat{V})$ , where  $\hat{V}$  is an hermitian operator in the  $N$  dimensional Hilbert space and  $\eta_z$  is the strength of the noise for a particular member of the ensemble  $\mathcal{E}_z$ . We take  $\langle \eta_z \rangle_z = 0$ , where  $\langle \cdot \rangle_z \Rightarrow \int (\cdot) p(z) dz$ , and  $p(z)$  is the probability of measuring the ensemble member labeled  $z$ . The fidelity decay after  $n$  iterations is the overlap of the ensemble average state  $\langle \tilde{\rho}_n \rangle_z$  and the ideal state  $\rho_n$

$$F_n = \langle \rho_n | \left\langle (\hat{P}_z \hat{S})^n | \rho_0 \right\rangle_z = \langle \rho_n | \langle \tilde{\rho}_n \rangle_z \rangle. \quad (3.5)$$

### 3.1.1 Decoherent noise

Decoherence describes a process whereby information is irreversibly lost to an environment. To model decoherent noise, we consider  $\eta_z$  to be random for a given member of the ensemble

on every iteration of the map. The random process is modeled by individually averaging the evolution of each member of the measurement ensemble  $\mathcal{E}_z$  over a stochastic ensemble  $\mathcal{E}_s$  that samples the distribution of random  $\eta_z$  values. The distribution of random  $\eta_z$  values satisfies  $\langle \eta_z \rangle_s = 0$ . The stochastic ensemble  $\mathcal{E}_s$  is averaged *before* the measurement ensemble  $\mathcal{E}_z$ .

We rewrite the input state  $\rho_0 = \frac{1}{N}\mathbb{1} + \chi\sigma_0$ , where  $\langle \mathbb{1}|\sigma_0 \rangle = 0$ ,  $\chi^2 = (N-1)/N^2$  and  $\text{trace}(\sigma_0^2) = N$  guarantee the normalization and purity of  $\rho_0$ . Now  $\hat{S}^n |\sigma_0 \rangle = |\sigma_n \rangle$ , where the unitarity of  $\hat{S}$  guarantees  $\langle \sigma_n | \mathbb{1} \rangle = 0$ . Our normalization conditions include  $\langle \sigma_n | \sigma_n \rangle = N$ . After the first iteration of the decoherent process

$$\begin{aligned} |\tilde{\rho}_1 \rangle &= \left\langle \hat{P}_z \hat{S} |\rho_0 \rangle \right\rangle_s = \left\langle \frac{1}{N} |\mathbb{1} \rangle + \chi \hat{P}_z |\sigma_1 \rangle \right\rangle_s \\ &= \left\langle \frac{1}{N} |\mathbb{1} \rangle + \chi (a_{01} |\sigma_1 \rangle + \mu_{01} |\sigma_{\mu 01} \rangle) \right\rangle_s, \end{aligned} \quad (3.6)$$

where we have decomposed  $\hat{P}_z |\sigma_1 \rangle$  into a component parallel to the ideal state  $|\sigma_1 \rangle$  and an orthogonal component  $|\sigma_{\mu 01} \rangle$  such that  $\langle \sigma_1 | \sigma_{\mu 01} \rangle = 0$  and  $a_{01}^2 + \mu_{01}^2 = 1$ . The value  $\mu_{01}$  is related to the strength of the noise such that for small errors  $\eta_z$ , we have  $\langle \mu_{01} \rangle_s = 0$ . Averaging over the stochastic ensemble  $\mathcal{E}_s$ , we have

$$|\tilde{\rho}_1 \rangle = \frac{1}{N} |\mathbb{1} \rangle + \chi \langle a_{01} \rangle_s |\sigma_1 \rangle. \quad (3.7)$$

If we allow the measurement ensemble  $\mathcal{E}_z$  and the stochastic ensemble  $\mathcal{E}_s$  to sample the same distribution  $p(z)$ , then we can define  $\alpha_{01} \equiv \langle a_{01} \rangle_s = \langle a_{01} \rangle_z$ . In this case, averaging  $\tilde{\rho}_1$  over  $\mathcal{E}_z$  has no effect, and  $\langle \tilde{\rho}_1 \rangle_z = \tilde{\rho}_1$ . For the decoherent model, the fidelity after one iteration of the perturbed map is

$$F_1^{(D)} = \langle \rho_1 | \langle \tilde{\rho}_1 \rangle_z \rangle = \frac{1}{N} + N\chi^2 \alpha_{01} = \frac{1}{N} + \frac{(N-1)}{N} \alpha_{01} \quad (3.8)$$

Now reiterating the process, the state after two iterations is

$$|\tilde{\rho}_2 \rangle = \left\langle \hat{P}_z \hat{S} |\tilde{\rho}_1 \rangle \right\rangle_s = \left\langle \frac{1}{N} |\mathbb{1} \rangle + \chi \alpha_{01} (a_{12} |\sigma_2 \rangle + \mu_{12} |\sigma_{\mu 12} \rangle) \right\rangle_s \quad (3.9)$$

and

$$F_2^{(D)} = \langle \rho_2 | \langle |\tilde{\rho}_2\rangle \rangle_z = \frac{1}{N} + \frac{(N-1)}{N} \alpha_{01} \alpha_{12}. \quad (3.10)$$

Since  $0 \leq \alpha_{j,j+1} < 1$ , the general expression for the fidelity decay under decoherent dynamics

$$F_n^{(D)} = \langle \rho_n | \langle |\tilde{\rho}_n\rangle \rangle_z = \frac{1}{N} + \frac{(N-1)}{N} \prod_{j=0}^{n-1} \alpha_{j,j+1} \quad (3.11)$$

is an exponentially decreasing function that saturates at  $1/N$ , as expected for a decoherent map.

### 3.1.2 Incoherent noise

Incoherence describes a process whereby information is reversibly encoded in the classical degrees of freedom of an ensemble by a static or slowly varying distribution of Hamiltonians. To model incoherent dynamics for a particular member of the measurement ensemble  $\mathcal{E}_z$ , we consider  $\eta_z$  to be a static value for each iteration of the map. In this case there is no stochastic ensemble; the local dynamics are deterministic and reversible. After one iteration of the incoherent map the state of an individual ensemble member is given by

$$|\tilde{\rho}_1\rangle = \frac{1}{N} |\mathbb{1}\rangle + \chi (a_{01} |\sigma_1\rangle + \mu_{01} |\sigma_{\mu 01}\rangle), \quad (3.12)$$

and so the ensemble-averaged state

$$\langle |\tilde{\rho}_1\rangle \rangle_z = \frac{1}{N} |\mathbb{1}\rangle + \chi \langle a_{01} \rangle_z |\sigma_1\rangle. \quad (3.13)$$

has a fidelity of

$$F_1^{(I)} = \frac{1}{N} + \frac{(N-1)}{N} \alpha_{01}, \quad (3.14)$$

which is equivalent to the value  $F_1^{(D)}$  measured in the decoherent case. The second iteration of the incoherent process returns the state

$$\begin{aligned} |\tilde{\rho}_2\rangle &= \hat{P}_z \hat{S} |\tilde{\rho}_1\rangle = \frac{1}{N} |\mathbb{1}\rangle + \chi \hat{P}_z (a_{01} |\sigma_1\rangle + \mu_{01} |\sigma_{\mu 01}\rangle) \\ &= \frac{1}{N} |\mathbb{1}\rangle + \chi a_{01} (a_{12} |\sigma_2\rangle + \mu_{12} |\sigma_{\mu 12}\rangle) + \chi \mu_{01} (b_{12} |\sigma_2\rangle + \nu_{12} |\sigma_{\nu 12}\rangle) \end{aligned} \quad (3.15)$$

where we have decomposed  $\hat{P}_z |\sigma_{\mu 01}\rangle$  into a component parallel to the ideal state  $|\sigma_2\rangle$  and an orthogonal component  $|\sigma_{\nu 12}\rangle$  such that  $\langle \sigma_2 | \sigma_{\nu 12} \rangle = 0$  and  $b_{12}^2 + \nu_{12}^2 = 1$ . Unlike the decoherent process, the incoherent process preserves the full  $|\sigma_{\mu 01}\rangle$  component after the first iteration. The second iteration of the map may then transform some portion of this component into the ideal state  $|\sigma_2\rangle$ . The possibility of fully “refocusing” errors in the incoherent case is the essential difference between decoherent and incoherent dynamics, and this difference is what leads to observable signatures of incoherence. Collecting terms, we have

$$\begin{aligned} |\tilde{\rho}_2\rangle &= \frac{1}{N} |\mathbb{1}\rangle + \chi (a_{01} a_{12} + \mu_{01} b_{12}) |\sigma_2\rangle + \chi (\mu_{01} \nu_{12} |\sigma_{\nu 12}\rangle + a_{01} \mu_{12} |\sigma_{\mu 12}\rangle) \\ &= \frac{1}{N} |\mathbb{1}\rangle + \chi (A_2 |\sigma_2\rangle + \Gamma_2 |\sigma_{\Gamma 2}\rangle), \end{aligned} \quad (3.16)$$

and in general we can write  $\tilde{\rho}_n$  as a pure state

$$|\tilde{\rho}_n\rangle = \left( \hat{P}_z \hat{S} \right)^n |\rho_0\rangle = \frac{1}{N} |\mathbb{1}\rangle + \chi (A_n |\sigma_n\rangle + \Gamma_n |\sigma_{\Gamma n}\rangle), \quad (3.17)$$

where  $\langle \sigma_n | \sigma_{\Gamma n} \rangle = 0$  and  $A_n^2 + \Gamma_n^2 = 1$ . Now after averaging over  $\mathcal{E}_z$ , the fidelity is given by

$$F_2^{(I)} = \frac{1}{N} + \frac{N-1}{N} (\langle a_{01} a_{12} \rangle_z + \langle \mu_{01} b_{12} \rangle_z) \quad (3.18)$$

$$F_n^{(I)} = \frac{1}{N} + \frac{N-1}{N} (\langle A_{n-1} a_{n-1,n} \rangle_z + \langle \Gamma_{n-1} b_{n-1,n} \rangle_z). \quad (3.19)$$

The first term in parenthesis  $\langle A_{n-1} a_{n-1,n} \rangle_z$  is similar to the term  $\prod_{j=0}^{n-1} \alpha_{j,j+1}$  in the expression for  $F_n^{(D)}$ , as they both cause the fidelity to decrease on each map iteration since  $0 \leq a_{n-1,n} < 1$ . However, the second term in parenthesis  $\langle \Gamma_{n-1} b_{n-1,n} \rangle_z$  may be nonzero and positive, allowing for an increase, or recurrence, in fidelity ( $F_n^{(I)} > F_{n-1}^{(I)}$ ) in some cases. As an example, consider the Carr-Purcell echo experiment where  $B_0$  field inhomogeneities



are fully refocused by  $\pi$  pulses. However, the recurrence in fidelity decay is more general than a simple echo experiment in which incoherence is inverted by local  $SU(2)$  operations. Recurrence in fidelity decay allows errors to be refocused from any part of Hilbert space through the repeated action of the perturbed map.

There is also a third type of noise that is not explicitly included in the model for incoherent or decoherent noise. Coherent noise causes non-ideal unitary errors that are uniform over the ensemble and do not cause a loss of purity in the individual ensemble members or in the ensemble-averaged state. In the noise models above, coherent errors could be incorporated by taking  $\langle \eta_z \rangle_z \neq 0$ . Like incoherent noise, coherent noise can cause recurrences in fidelity decay. However, there is little motivation to distinguish them in this setting since the two types of noise can be treated with the same techniques, which do not require access to a larger Hilbert space.

Recurrences in a fidelity decay are a unique signature of microscopically reversible dynamics. For the case that  $\hat{S}$  is an entangling operation, incoherent errors will cause a loss in the purity of the ensemble that is not recovered by single-qubit operations, and therefore is difficult to distinguish from the effects of decoherence. Fidelity decay under imperfect motion reversal provides an efficient means for observing signatures of incoherence even in the presence of an entangling operation.

## 3.2 Experiment

**Quantum Circuit.** Figure 3-1 shows the quantum circuit used to study incoherence in an entangling operation. This circuit is an example of a case where incoherence causes errors in the output state that are not easily distinguished from the effects of decoherence. The first three gates in the circuit create the GHZ state  $(|000\rangle + |111\rangle) / \sqrt{2}$ . Next, an entangling operation on qubits two and three is repeated  $4n$  times. The final three gates convert the resulting entangled state to a separable computational basis state. For odd values of  $n$  the final state is  $|001\rangle$ , and for even values of  $n$  the final state is  $|000\rangle$ . Incoherent noise in the repeated entangling operation will propagate through the Hilbert space, creating entangled components in the final state. These errors cause a loss of purity that mimics decoherence since they are not refocused by inverting the incoherence on the output state.

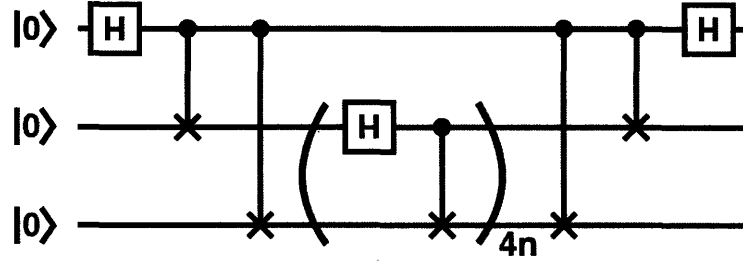


Figure 3-1: The quantum circuit for exploring incoherence in an entangling operation on a QIP. H represents the single-qubit Hadamard operation  $(\sigma_z + \sigma_x)/\sqrt{2}$ , the two-qubit gate represents a controlled-not operation, which flips the target qubit when the control qubit is in the  $|1\rangle$  state. The first three gates create a maximally entangled GHZ state  $(|000\rangle + |111\rangle)/\sqrt{2}$ , which is followed by  $4n$  iterations of a two-qubit entangling operation. The final three gates convert the resulting entangled state to the computational basis state  $|000\rangle$  for even values of  $n$  and  $|001\rangle$  for odd values of  $n$ . Incoherence in an entangling operation mimics decoherence by causing a loss of purity that is not refocused in the output state by inverting the incoherence. In our experiment, we observe signatures of incoherence in the two-qubit entangling operation by measuring the fidelity decay of the output state for  $n=0$  through 30.

**NMR QIP.** In NMR quantum information processing, nuclear spins polarized by a strong external magnetic field serve as qubits. The molecule used in this experiment, diagrammed in Fig. 3-2, is tris(trimethylsilyl)silane-acetylene dissolved in deuterated chloroform. The carbon nuclei in the acetylene branch are isotopically enriched  $^{13}\text{C}$ , while the methyl carbons are of natural isotopic abundance. The two carbon-13 nuclei and the hydrogen nucleus in the acetylene branch are used as qubits. The full internal Hamiltonian of the nuclear spin system has the form

$$\mathcal{H}_{int} = \sum_{j=1}^{n_q} \pi \nu_j \sigma_z^j + \sum_{j < k} \frac{\pi J_{jk}}{2} \sigma^j \cdot \sigma^k \quad (3.20)$$

where  $\nu_j$  is the resonance frequency of the  $j^{\text{th}}$  spin, and  $J_{jk}$  is the frequency of scalar coupling between spins  $j$  and  $k$ . The hydrogen nucleus is labeled qubit number 1, making it the most significant bit in the computational state vector. The repeated entangling operation is applied to the carbon qubits, which are labeled as indicated in Fig. 3-2. Experiments are performed in a 9.4 Tesla magnetic field, where the Carbon qubits are separated by 1.201 kHz. The scalar couplings are  $J_{12} = 235.7$  Hz,  $J_{23} = 132.6$  Hz, and  $J_{13} = 42.9$  Hz.

The initial pseudopure state [20] was created by the technique described in [104] using hard rf pulses and gradient fields. The input state preparation pulse sequence, which is

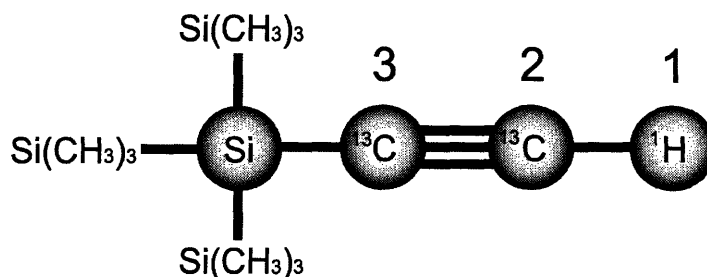


Figure 3-2: A diagram of the tris(trimethylsilyl)silane-acetylene molecule used to implement the quantum circuit in Fig. 3-1 in a liquid state NMR QIP. The two-qubit entangling operation is applied to the two  $^{13}\text{C}$  spins in the acetylene branch, labeled qubits 2 and 3. The primary source of incoherence in the experimentally implemented entangling operation is the inhomogeneity of the carbon rf control field.

non-unitary, was optimized based on the state correlation [37] between the numerically simulated input state and the ideal input state. The average gate fidelities [37] of the sequences corresponding to the three sections of the circuit were optimized over the full Hilbert space. In the experiment, representative measurements of the fidelity are taken. A single  $\pi/2$  readout pulse on the hydrogen spin was used to measure the  $\sigma_z^1$ ,  $\sigma_z^1\sigma_z^2$ ,  $\sigma_z^1\sigma_z^3$ , and  $\sigma_z^1\sigma_z^2\sigma_z^3$  components of the output density matrix, for  $n = 1$  through  $n = 30$ .

### 3.3 Numerical simulation

The NMR experiment was numerically simulated on a classical computer. The dominant incoherent noise in the experiment arises due to the inhomogeneity of the rf control field over the spatial extent of the liquid state NMR sample. When an rf pulse is applied during the experiment, the members of the ensemble experience a distribution of rf powers, and only a fraction of the ensemble actually experiences precisely the nominal (ideal) rf power. While the control fields for both the hydrogen and carbon qubits are known to be inhomogeneous, the inhomogeneity of the carbon control field is the dominant source of incoherent errors in the entangling operation. Consequently, our numerical simulations include incoherence for each carbon pulse as a distribution of rf control field strengths. The discrete nine-point distribution used in simulations is plotted in Fig. 3-3. The natural decoherence of the nuclear spin system is simulated by an approximate relaxation superoperator [35], which is completely diagonal in the generalized Pauli basis. In this diagonal form, each non-zero

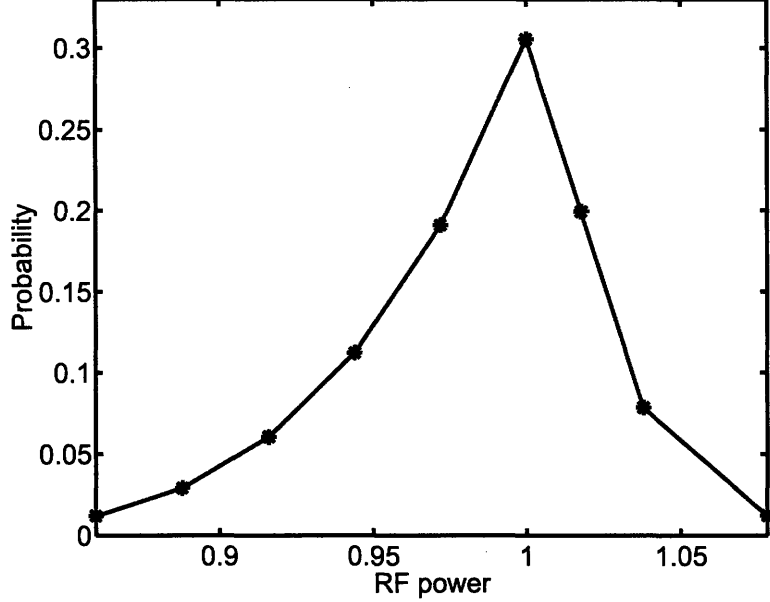


Figure 3-3: The distribution of carbon rf powers measured in previous experiments and used in numerical simulations of the NMR implementation of the circuit in Fig. 3-1. The rf power is in units of the nominal rf nutation frequency (17.5 kHz).

entry in the relaxation superoperator represents the decoherence rate of a generalized Pauli basis operator; the specific values used in simulations are based on measurements of all T1s and the single species T2s.

In numerical simulations, we are interested in the unique features of fidelity decay caused by incoherence. This is accomplished by separating out those parts of the evolution that are uniform over the ensemble. We isolate the effects of incoherence by simulating the rf inhomogeneity in two regimes of dynamics. In the incoherent model, rf inhomogeneity is simulated as it actually occurs in the experiment, as a static distribution of local unitary noise. The output state in this regime is  $\left\langle \left( \hat{P}_z \hat{S} \right)^n | \rho_0 \right\rangle_z$ . In this model, the full state of each ensemble member is preserved between iterations, which leads to recurrences in fidelity as discussed in Sec. 3.1.2. In the decoherent model, rf inhomogeneity is simulated fictitiously as a stochastic effect, as discussed in Sec. 3.1.1. The output state in this regime is  $\left( \left\langle \hat{P}_z \hat{S} \right\rangle_z \right)^n | \rho_0 \rangle$ . In this model, averaging the state after each iteration preserves only an average state that is uniform over the ensemble. Differences between the two models arise purely from incoherence. We emphasize that rf inhomogeneity is known to be a static effect, and the fictitious stochastic model is used only to isolate the signatures of incoherence. We also note that the relaxation superoperator, a well-understood source of decoherent noise,

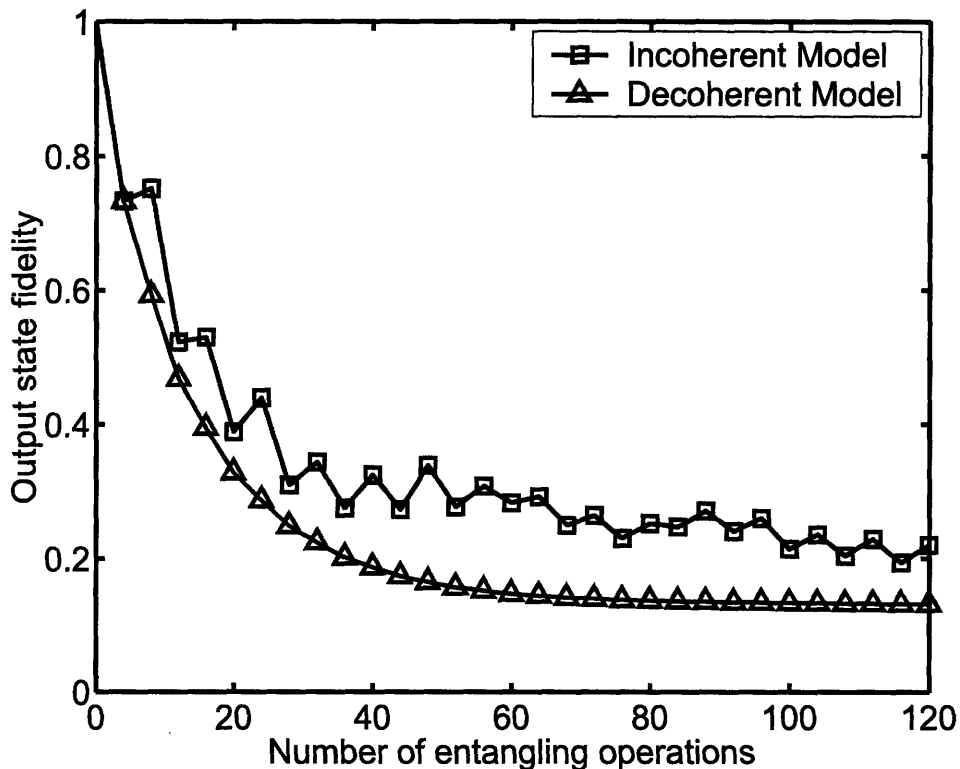


Figure 3-4: The fidelity decay from a numerical simulation of the experiment, where rf inhomogeneity (RFI) is simulated using two different models. RFI is simulated as a static distribution in the incoherent model, while RFI is fictitiously simulated as a stochastic effect in the decoherent model. This fiction allows us to isolate signatures of incoherence. In the incoherent model, fidelity recurrences (which appear as oscillations in the plot) are observed because the purity of the ensemble members is preserved and the repeated action of the entangling map refocuses some of the errors. There are no significant recurrences in the decoherent model because the individual members of the ensemble lose purity, the errors are not refocused, and the fidelity decays steadily and saturates. Comparison of the two plots shows that the fidelity decay recurrences are caused by incoherent noise.

is simulated identically in both models.

The results of numerical simulations are plotted in Fig. 3-4. Although incoherence in entangling operations creates a loss of purity that mimics decoherence, fidelity decay under imperfect reversal of such a process reveals distinguishable properties of the incoherence. The first point in the two fidelity decays are identical, as predicted in Sec. 3.1.2. However, differences in the two models are manifest already in the second point of the fidelity decay, as the fidelity increases only in the incoherent model. Over 120 entangling operations, the numerically simulated fidelity decay for the incoherent case shows rapid oscillations, or recurrences, which are only possible for microscopically reversible dynamics, as discussed in

Section 3.1.2. The decoherent simulation shows a non-oscillatory decay and saturation at a value of the inverse of the dimension of the Hilbert space  $1/N$ . Differences between the fidelity decays collected in the two regimes reveal a signature of incoherent noise which is also observed in experimental data.

### 3.4 Results and discussion

Experimental data resulting from an implementation of the optimized control sequences are compared to results of numerical simulations of the experiment for the two models of rf inhomogeneity previously discussed. Rf inhomogeneity is simulated as a static distribution in the incoherent model, while rf inhomogeneity is fictitiously simulated as a stochastic effect in the decoherent model. The fictitious model of a stochastic distribution of rf powers isolates the effects of incoherence from evolution that is uniform over the ensemble. Figure 3-5 shows the sum of the measured magnitudes of four state components ( $\sigma_z^1$ ,  $\sigma_z^1\sigma_z^2$ ,  $\sigma_z^1\sigma_z^3$ , and  $\sigma_z^1\sigma_z^2\sigma_z^3$ ) obtained by experiment and by numerical simulations. Under the ideal unitary evolution, the value of the plotted sum is 0.5. The experimentally observed value decreases for about 24 iterations of the entangling operation, and then begins to oscillate and later becomes nearly constant. The incoherent model reproduces the important features of the experimental data. The value simulated by the incoherent model oscillates over many iterations, and finally settles to a nearly constant value. By contrast the value simulated by the decoherent model decreases rapidly and steadily, never oscillates, and saturates to zero. This comparison demonstrates that incoherence in the entangling operation appears with distinct signatures in the experimental data.

Some insight is gained by comparing the the individually measured state components of the density matrix ( $\sigma_z^1$ ,  $\sigma_z^1\sigma_z^2$ ,  $\sigma_z^1\sigma_z^3$ , and  $\sigma_z^1\sigma_z^2\sigma_z^3$ ) in the frequency domain by Fourier transforming the data, as plotted in Fig. 3-6. In each set of axes, the frequency is represented on the horizontal axis in units of oscillation periods per entangling operation. The highest observable (Nyquist) frequency is  $1/8$ , since the state was measured after every four entangling operations. Comparing the experimental data with the two types of simulation, we see again that the incoherent model of rf inhomogeneity accurately reproduces key features of the experimental data which are not reproduced by the decoherent model. The dominant signal in all twelve plots is the zero frequency peak, which is caused by the initial decline

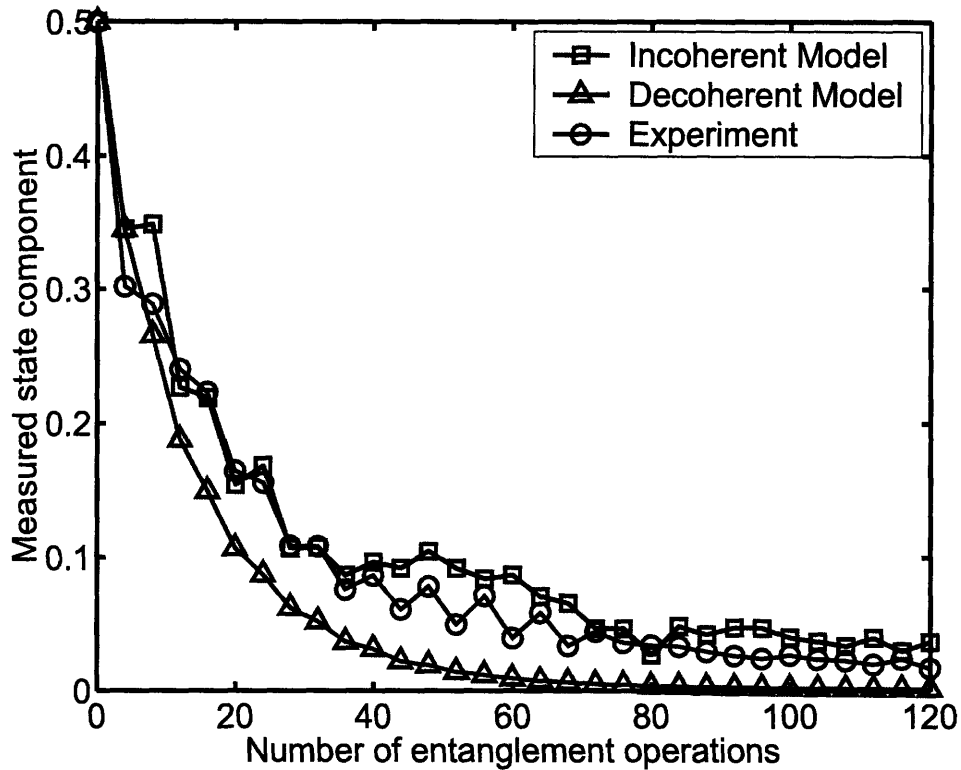


Figure 3-5: The sum of the absolute value of the density matrix components measured in the experiment and in numerical simulations. This measurement is a representative measure of state fidelity for the map under consideration. If inhomogeneity is numerically simulated using an incoherent model and a fictitious decoherent model as discussed in the text. For the ideal map with no noise, the sum of the density matrix components is a constant value of 0.5. Experimental noise and decoherence cause the measured value to initially decrease. However, as the map is iterated, the measured value increases and begins to oscillate. This behavior is well-reproduced by the incoherent model, while the decoherent model does not predict the oscillatory behavior. This plot shows that incoherence in the entangling operation appears with distinct signatures in the experimental data.

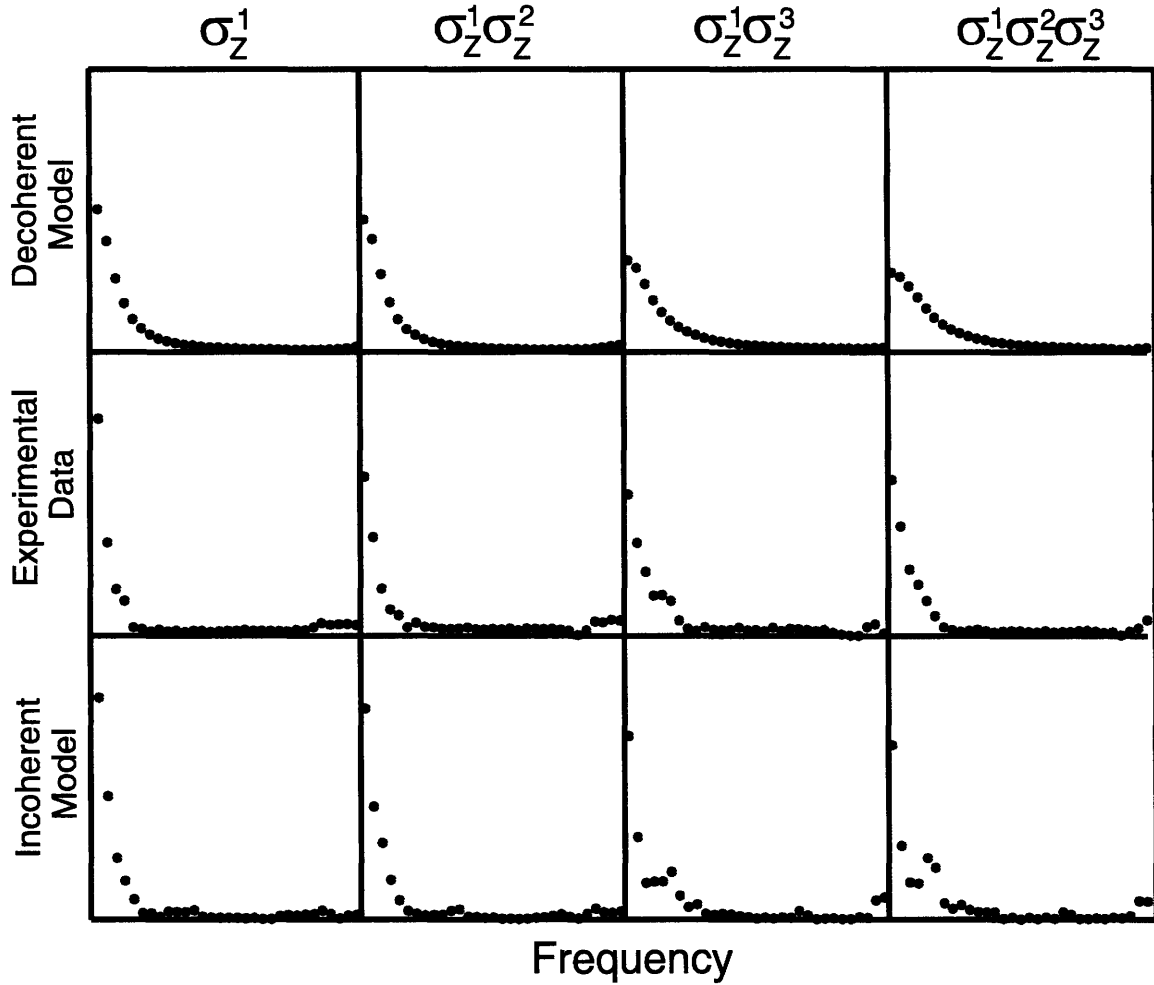


Figure 3-6: The Fourier transform of each experimentally measured component of the density matrix (middle row), compared to numerical simulations of the experiment using two models of rf inhomogeneity discussed in the text. The horizontal axis represents frequency in units of oscillation periods per entangling operation, with values ranging from 0 (left) to 1/8 (right). Resolved high frequency components, which represent fidelity recurrences, are observed in the experimental data and in numerical simulations of the incoherent model, but not in numerical simulations of the decoherent model. The dominant high frequency components are observed in the three-body term  $\sigma_z^1\sigma_z^2\sigma_z^3$  at the Nyquist frequency. This plot shows that incoherence in the experimentally implemented entangling operation appears as high frequency components in the Fourier transform of a state fidelity measurement.



in fidelity observed for all three plots in Fig. 3-5. The zero frequency peak is somewhat broader in the decoherent model, which reflects the rapid decay to zero of that data in the time-domain. The important features in the time-domain data, namely the oscillatory fidelity recurrences, are represented in the high frequencies of the Fourier domain. The oscillatory behavior in the experimental data and in the incoherent model simulations in Fig. 3-5 appear as resolved high frequency components of the individual state measurements in Fig. 3-6. The largest high frequency component occurs in the  $\sigma_z^1 \sigma_z^2 \sigma_z^3$  measurement at the Nyquist frequency.

Incoherence in an entangling operation causes a loss of purity over the ensemble that is not recovered by an inverted incoherent process, and therefore is difficult to distinguish from decoherence. However, incoherence due to inhomogeneity in the rf control field during the implemented entangling operation appears as a distinct process in our experimental data in the form of fidelity recurrences. Numerical simulations are used to identify the recurrences as a purely incoherent effect. Incoherent errors are isolated in numerical simulations by separating out those parts of the evolution that are identical over the ensemble in a fictitious decoherent model, and we see that the decoherent process does not give rise to fidelity recurrences.

### 3.5 Conclusions

We have shown that incoherence can lead to recurrences in a fidelity decay, whereas decoherence cannot lead to such behavior, which provides an efficient framework for identifying signatures of incoherence. In our experiment, a two-qubit entangling operation was repeated 120 times on a three-qubit GHZ state in a liquid state NMR QIP, and fidelity recurrences in the experimental data were created by incoherence due to inhomogeneity of the rf control field. The experiment was numerically simulated modeling rf inhomogeneity in two regimes: as a static distribution of Hamiltonians and fictitiously as a stochastic distribution of Hamiltonians. The stochastic model mimics a decoherent process, allowing us to isolate the incoherent effects of rf inhomogeneity. The comparison identifies the experimentally observed recurrences as an incoherent process. The approach for detecting incoherence described here will be a valuable resource in QIPs operating in larger Hilbert spaces with entangled states over many qubits, where the effects of incoherence and decoherence are

difficult yet important to distinguish.

## Chapter 4

# Liquid crystal solvent NMR QIPs

Some materials exhibit a liquid crystal phase, or mesophase, which has properties of both liquid and solid phases. Liquid crystals are like liquids in that the constituent molecules undergo rapid translational diffusion, and they are like solids in that the molecules demonstrate some amount of long-range ordering. The particular nature of the microscopic ordering varies among materials, but the most commonly observed type of ordering is the nematic mesophase. Nematic materials are typically made of long, rod-like organic molecules which, in nematic mesophase temperature regimes, prefer to self-align as illustrated in Figure 4-1. When a sample of nematic mesophase material is subject to a uniform external magnetic field, the field acts as a director for the aligned particles, and the material adopts molecular orientational preferences which are uniform over the sample [29, 34].

### 4.1 NMR with liquid crystal solvents

The NMR spectrum of a typical nematic liquid crystal material is very broad and has little structure. These characteristics arise due to the presence of many non-equivalent dipolar-coupled protons in the liquid crystal material. By contrast when a smaller, rigid molecule is dissolved in a liquid crystal, the solute adopts the orientational ordering of the solvent, and a resolved NMR spectrum is observed. The resolved peaks of the solute spectrum appear with a broad baseline due to the liquid crystal material, as seen in Figure 4-2(a). The figure shows the proton spectrum of *o*-chloronitrobenzene (CNB) partially oriented by the liquid crystal solvent ZLI-1132 at 600 MHz. The resolved peaks are from the four protons of CNB, and the baseline modulation arises from the many non-equivalent dipolar-coupled protons

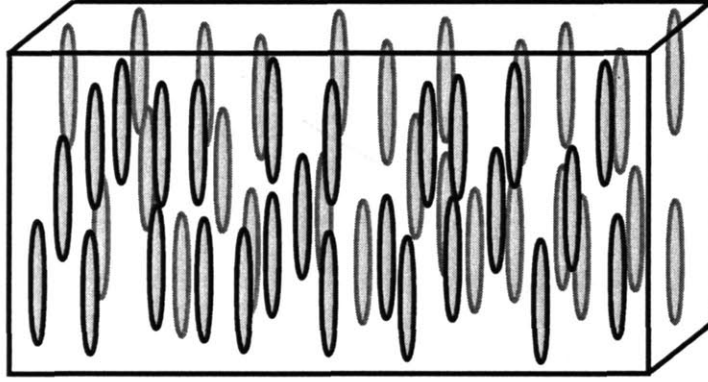


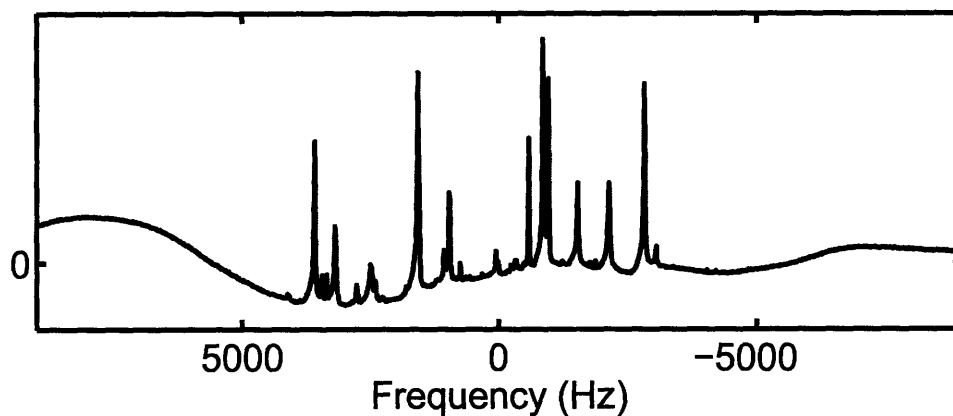
Figure 4-1: Illustration of the order properties of a nematic liquid crystal phase, showing orientational but not positional ordering. The material is composed of long, rod-like molecules that become self-aligned at certain temperatures. When the nematic phase is subject to an external magnetic field, the field acts as a director for the molecular alignment. Solute dissolved in a nematic liquid crystal adopt preferred orientations that restrict thermal rotation, causing nuclear spins within the molecule to retain non-zero dipolar interactions which are not present in an isotropic liquid. The intramolecular dipolar couplings are useful for NMR quantum information processing.

of ZLI-1132.

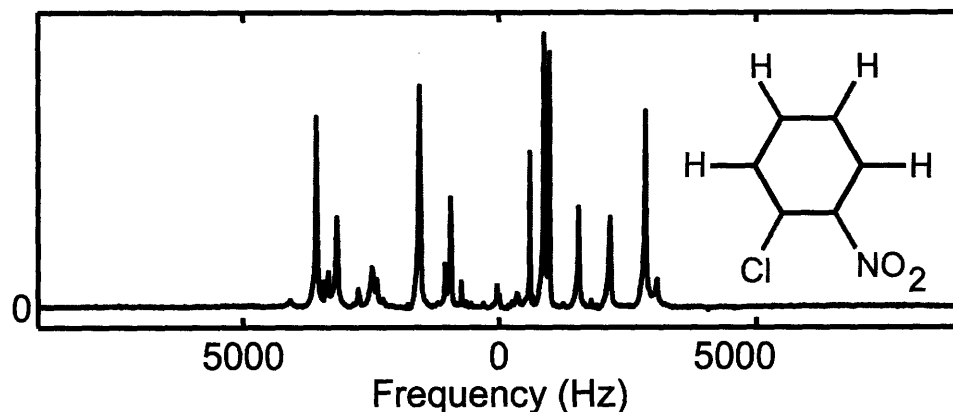
The baseline due to the liquid crystal solvent can be removed by inserting a time suspension sequence, such as the Cory-48 pulse sequence [22], before acquiring an FID. This technique works because the dipolar coupling of the liquid crystal solvent spins, whose signal we want to suppress, is much stronger than the dipolar coupling of the solute spins, whose signal we want to observe ( $d_{supp} \gg d_{obs}$ ). By selecting a pulse sequence that refocuses the solute spins ( $\tau d_{obs} \ll 1$ ) but not the solvent spins ( $\tau d_{supp} \gg 1$ ), the unwanted signal is removed. In our experiments we found that one cycle of the Cory-48 pulse sequence, using  $\tau = 30\mu s$  and a  $(\pi/2)$  pulse time of  $6.85\mu s$ , worked well. The results of the baseline suppression technique for CNB dissolved in ZLI-1132 are shown in Figure 4-2(b).

After removing the baseline, we are left with a complicated spectrum of many resolved transitions. The dominant features in the resolved spectrum arise due to the presence of strong magnetic dipolar couplings among nuclear spins in the solute material. This strong dipolar interaction is the principal difference between liquid and liquid crystal solvent NMR. The secular homonuclear dipolar interaction between two spins ( $j$  and  $k$ ) in a strong magnetic field is given by

$$\mathcal{H}_{Dip}^{jk} = \frac{D_{jk}}{2} \left( 2\sigma_z^j \sigma_z^k - \sigma_x^j \sigma_x^k - \sigma_y^j \sigma_y^k \right) \quad (4.1)$$



(a) NMR spectrum after  $\pi/2$  pulse



(b) NMR spectrum after  $\pi/2$  pulse and Cory-48 pulse sequence

Figure 4-2: 600 MHz proton spectrum of o-chloronitrobenzene (CNB) partially oriented by the liquid crystal solvent ZLI-1132. (Top) The spectrum after a single ( $\pi/2$ ) pulse features a broad baseline due to the liquid crystal solvent, which contains many nonequivalent strongly dipolar-coupled protons. The resolved peaks are the four dipolar coupled protons of the CNB solute material. The dipolar coupling among solvent protons is much stronger than among solute protons. (Bottom) The spectrum after a ( $\pi/2$ ) pulse and one cycle of the Cory-48 pulse time suspension sequence ( $\tau = 30\mu\text{s}$ ,  $\pi/2$  pulse =  $6.85\mu\text{s}$ ). The baseline is suppressed because the pulse sequence is parameterized to refocus the dipolar couplings among solute protons but not among solvent protons.

where  $D_{jk}$  is the dipolar coupling strength (in units of Hz)

$$D_{jk} = \left( \frac{\mu_0 \hbar \gamma_j \gamma_k}{8\pi^2} \right) \left( \frac{1 - 3 \cos^2 \theta_{jk}}{r_{jk}^3} \right), \quad (4.2)$$

$r_{jk} = \|\vec{r}_{jk}\|$  is the length of the internuclear vector,  $\theta_{jk}$  is the angle between the internuclear vector and the  $B_0$  field,  $\mu_0$  is the permeability of free space, and  $\hbar$  is Planck's constant divided by  $2\pi$ . The value of the expression in the first set of parenthesis in equation (4.2) is determined by the type of nuclear species; for two protons  $(\mu_0 \hbar \gamma_j \gamma_k / 8\pi^2) = 120 \text{ kHz } \text{\AA}^3$ .

For an ensemble of rigid molecules, the internuclear distances are fixed by the structure of the molecule, and the angular terms in the dipolar coupling strength are averaged over the distribution of molecular orientations in the ensemble

$$d_{jk} = \left( \frac{\mu_0 \hbar \gamma_j \gamma_k}{8\pi^2 r_{jk}^3} \right) \langle 1 - 3 \cos^2 \theta_{jk} \rangle, \quad (4.3)$$

where the angular brackets denote the ensemble average. In both liquid and liquid crystal solvents, the solute molecules move about with rapid, diffusive translational motion, which averages the intermolecular dipolar couplings to zero. In addition to translational motion, the molecules in a liquid are randomly rotating, averaging out the intramolecular dipolar couplings as well. By contrast, a molecule dissolved in a liquid crystal has a preferred orientation, so rotational motion is restricted, and intramolecular dipolar couplings are retained, as the bracketed term in equation (4.3) averages to some non-zero value.

## 4.2 Dipolar coupling in a partially oriented system

Emsley and Lindon's text [34] gives a detailed derivation of the effective NMR dipolar Hamiltonian for partially oriented systems. The observed nuclear dipolar couplings arise from an ensemble average over the distribution of molecular orientations. The order parameter  $S_{\alpha\beta}$  provides a convenient framework for representing the ensemble averaging. In general, the order parameter varies with temperature and depends heavily on the liquid crystal solvent and the symmetry of the solute molecule. In order to express the observed dipolar couplings in terms of the order parameter, we first define two Cartesian coordinate systems. The lab frame coordinate axes are labeled x, y, and z, and the molecular frame coordinate axes are labeled a, b, and c. The lab frame is defined by the external  $B_0$  field,

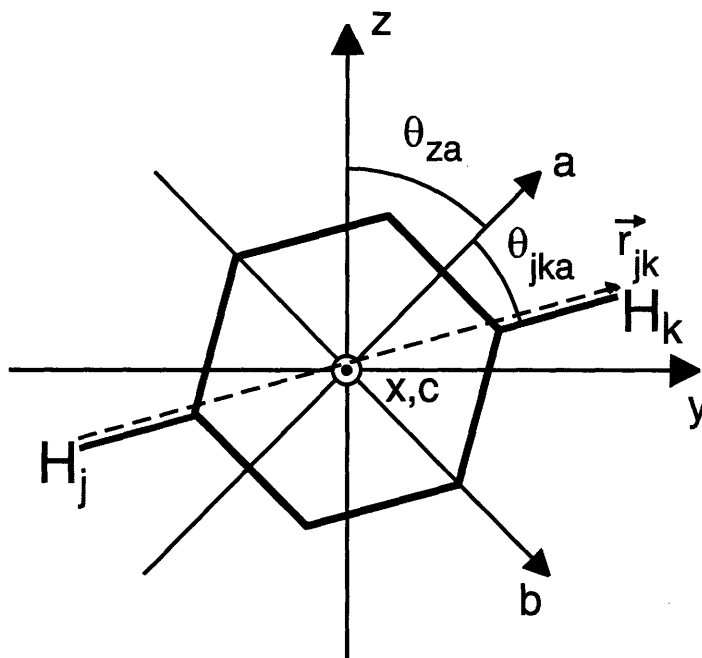


Figure 4-3: Coordinate frames used in the expression of the order parameter. The molecule is fixed in the molecular frame, whose axes are labeled a, b, and c. Thermal energy causes the molecular frame to rotate with respect to the lab frame, whose axes are labeled x, y, and z. The z-axis is parallel to the external  $B_0$  field; the x- and c-axes are perpendicular to the yz-plane. The internuclear vector  $\vec{r}_{jk}$  makes an angle  $\theta_{jka}$  with the molecular a-axis. The molecular a-axis makes an angle  $\theta_{za}$  with the lab z-axis. The order parameter given in equation (4.4) describes the distribution of molecular frame orientations in an ensemble of molecules. Equation (4.5) relates the order parameter to the observed dipolar couplings  $d_{jk}$ .

which is parallel to the z-axis. The molecular frame is defined by the orientation of the molecule, as the molecule is fixed in the molecular frame. The indices  $\alpha$  and  $\beta$  will be used to represent a generic axis in the molecular frame. The order parameter is expressed

$$S_{\alpha\beta} = \frac{1}{2} \langle 3 \cos \theta_{\alpha z} \cos \theta_{\beta z} - \delta_{\alpha\beta} \rangle \quad (4.4)$$

where the angled brackets indicate the ensemble average,  $\delta_{\alpha\beta}$  is the Kronecker delta, and  $\theta_{\alpha z}$  is the angle between the lab z axis and the molecular  $\alpha$  axis. These angles and their relationship to the lab and molecular frames are illustrated in Figure 4-3 for a benzene molecule. The effective dipolar couplings for a partially oriented system can now be expressed

$$d_{jk} = \left( \frac{\mu_0 \hbar \gamma_j \gamma_k}{8\pi^2 r_{jk}^3} \right) \sum_{\alpha\beta} S_{\alpha\beta} \langle \cos \theta_{jk\alpha} \cos \theta_{jk\beta} \rangle \quad (4.5)$$

where  $\theta_{jk\alpha}$  is the angle between the internuclear vector  $\vec{r}_{jk}$  and the molecular  $\alpha$ -axis, illustrated in Figure 4-3. In a liquid, all elements of  $S_{\alpha\beta}$  are zero, and there is no dipolar coupling.

The order parameter is a traceless rank-two tensor, so the diagonal elements are often expressed as two independent terms  $S_{aa}$  and  $(S_{bb} - S_{cc})$ . Also, because  $S_{\alpha\beta}$  is symmetric, the off-diagonal terms can be reduced to three independent terms  $S_{ab}$ ,  $S_{ac}$  and  $S_{bc}$ . In this representation, the dipolar couplings are given by

$$\begin{aligned} D_{jk} = \left( \frac{\mu_0 \hbar \gamma_j \gamma_k}{8\pi^2 r_{jk}^3} \right) & [S_{aa} \langle \cos^2 \theta_{jka} \rangle + (S_{bb} - S_{cc}) \langle \cos^2 \theta_{jkb} - \cos^2 \theta_{jkc} \rangle \\ & + 2S_{ab} \langle \cos \theta_{jka} \cos \theta_{jkb} \rangle + 2S_{ac} \langle \cos \theta_{jka} \cos \theta_{jkc} \rangle \\ & + 2S_{bc} \langle \cos \theta_{jkb} \cos \theta_{jkc} \rangle]. \end{aligned} \quad (4.6)$$

which is often used in literature and texts. The order parameter is a convenient representation of the ensemble average orientation because it characterizes the molecular orientation in the molecular frame. The molecular frame can be chosen to exploit symmetries in the molecule, which reduces the number of independent parameters necessary to characterize molecular motion in the molecular frame. Consequently, the order parameter can often be reduced to fewer than five independent terms. For example, the symmetry of the benzene molecule reduces the order parameter to a single nonzero term  $S_{aa}$ . The proton NMR spectrum of benzene partially oriented by the liquid crystal ZLI-1132 is shown in Figure 4-4. The symmetry of the spectrum is a result of the benzene molecule's symmetry.

Now the internal Hamiltonian of the solute spin system can be written

$$\mathcal{H} = \sum_j \pi \nu_j \sigma_z^j + \sum_{j < k} \frac{\pi}{2} (J_{jk} + 2d_{jk}) \sigma_z^j \sigma_z^k + \sum_{j < k} \frac{\pi}{2} (J_{jk} - d_{jk}) (\sigma_x^j \sigma_x^k + \sigma_y^j \sigma_y^k) \quad (4.7)$$

where  $\nu_j$  is the resonance frequency of the  $j^{\text{th}}$  spin,  $d_{jk}$  is the dipolar coupling strength (modified by  $S_{\alpha\beta}$ ) between spins  $j$  and  $k$ , and  $J_{jk}$  is the corresponding scalar coupling strength. In liquid crystal solvent systems, dipolar coupling strengths can reach a few kilohertz. For a given pair of spins the dipolar coupling is typically one to two orders of



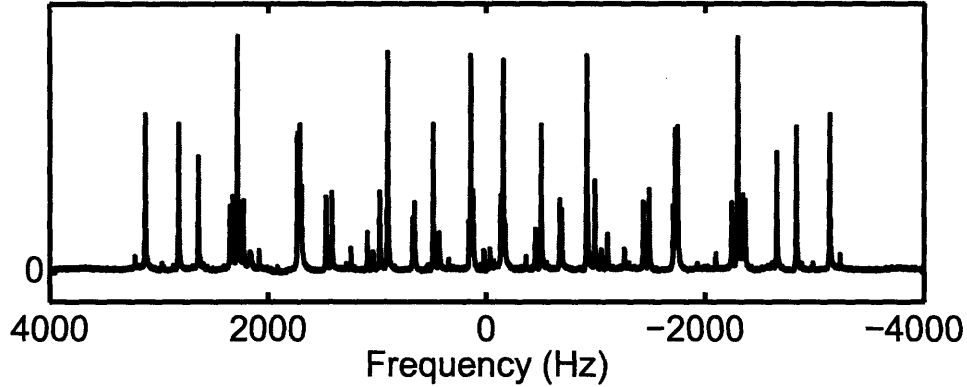


Figure 4-4: 600 MHz proton spectrum of benzene partially oriented by the liquid crystal solvent ZLI-1132. The symmetry of the NMR spectrum is a result of the symmetry of the benzene molecule. The order parameter for this system has one independent parameter which uniformly scales the dipolar couplings among all six protons and therefore determines the spectral breadth.

magnitude larger than the scalar coupling.

For ordered systems, the chemical shift difference between two nuclear spins  $\Delta\nu_{jk} = |\nu_j - \nu_k|$  is often smaller than or comparable to the dipolar coupling strength  $d_{jk}$ , so we have  $\Delta\nu_{jk} \approx d_{jk}$ . This contrasts with the liquid state, where typically  $d_{jk} = 0$  and  $\Delta\nu_{jk} \gg J_{jk}$ . The effect is that the nuclear Zeeman energy levels in the partially ordered system are mixed by the anisotropic coupling terms of the internal Hamiltonian. The peak heights and positions in the resulting NMR spectrum are affected by the mixing, and the physical parameters of the internal Hamiltonian are not trivially extracted from the NMR spectrum, as they usually can be in liquid state systems.

### 4.3 Liquid crystal solvent NMR QIPs

The solute material in a liquid crystal solvent system can be used for NMR quantum information processing to some advantage over liquid state systems [120]. One primary advantage is a direct result of the large dipolar couplings in partially oriented systems. The computing speed of an NMR quantum processor is related to the inverse of the nuclear spin coupling strength, and therefore the computing speed of a liquid crystal solvent NMR QIP (LNQ) is much faster than that of a liquid state system. Another advantage is the greater availability of molecules bearing large networks of strongly coupled nuclear spins. In order to perform conditional quantum logic gates, the nuclear spins in an NMR QIP

must exchange information. Nuclei in the liquid state exchange information by through-bond scalar couplings, so nuclei that are not directly bonded must exchange information indirectly, traversing multiple bonds. Dipolar coupling is a spatial effect, and in a partially ordered system, even distant nuclei that are not directly bonded can directly exchange information, simplifying multiple-qubit quantum logic gates. In addition, the coherence times of nuclear spins in an LNQ can be hundreds of milliseconds long, providing sufficient time to perform many quantum logic operations before the system decoheres.

**From liquids to solids** There are additional reasons, other than their performance, for developing coherent control in LNQs. The future direction of NMR quantum information processing (discussed in Chapter Six), aspires to implement coherent control in large Hilbert spaces using solid state devices. However, adapting the tools of liquid state NMR QIPs to these systems is not a trivial task. Figure 4.3 shows how LNQs fit into the broad picture of NMR quantum information processing as a bridge from liquid to solid state implementations. The left and middle columns of the figure illustrate liquid crystal as a *mesophase* of matter, in the *middle* of a liquid and solid phase. The third column of Figure 4.3 shows that the nuclear spin dynamics of an LNQ are in a *meso*-regime between liquid state and solid state dynamics. Liquid state dynamics are typically dominated by the Zeeman interaction ( $\Delta\nu_{jk} \gg J_{jk}$ ,  $d_{jk} = 0$ ), whereas solid state dynamics are typically dominated by the dipolar interaction ( $\Delta\nu_{jk} \ll d_{jk}$ ). Materials dissolved in a liquid crystal are typically in a regime between these two extrema ( $\Delta\nu_{jk} \approx d_{jk}$ ). From this perspective, LNQs provide a natural setting for translating liquid state methodologies to dipolar coupled systems and for addressing some of the other important challenges in solid state NMR quantum information processing.

**Challenges** Just as the advantages of LNQs arise due to the presence of strong dipolar couplings, so do the some of the challenges. LNQs provide moderately large networks of dipolar-coupled nuclear spins, and a significant challenge in these systems is to characterize and coherently control the dipolar interaction. Multiple pulse techniques and magic angle spinning have both been used with great success to effectively average out the dipolar Hamiltonian [43, 77]. Other work has demonstrated coherent control in dipolar coupled systems [4, 5, 73, 89]. However, as the number of spins increases, the size of the Hilbert

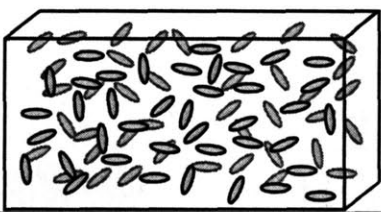
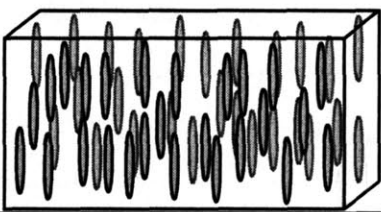
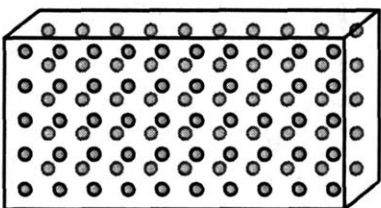
	<p style="text-align: center;"><b>Liquids</b></p> <ul style="list-style-type: none"> <li>-translational diffusion</li> <li>-random reorientation</li> </ul>	$\Delta\nu \gg J_{jk}$ $d_{jk} = 0$ up to 12 qubits
	<p style="text-align: center;"><b>Liquid Crystals</b></p> <ul style="list-style-type: none"> <li>-translational diffusion</li> <li>-partially oriented</li> </ul>	$\Delta\nu \approx d_{jk}$ $d_{jk} \neq 0$ 15-30 qubits
	<p style="text-align: center;"><b>Solids</b></p> <ul style="list-style-type: none"> <li>-no diffusion</li> <li>-highly ordered</li> </ul>	$\Delta\nu \ll d_{jk}$ $d_{jk} \neq 0$ many qubits

Figure 4-5: Comparison of three regimes of NMR QIP, showing liquid crystal solvent NMR QIPs as a bridge between liquid and solid state implementations. Liquid state NMR QIPs explore coherent control with a small number of weakly coupled nuclear spins. Solids host large networks of strongly dipolar-coupled nuclear spins, an attractive setting for implementing coherent control of large Hilbert spaces. Liquid crystal solvent systems provide a middle-ground, where the dynamics approach solid state conditions, and the available Hilbert spaces are larger than those available in the liquid state. LNQs provide a natural setting for addressing some of the important challenges in solid state NMR quantum information processing.

space grows exponentially, and pushing coherent control techniques to large Hilbert space implementations remains a significant challenge. Another effect of increasing the number of dipolar coupled spins in an LNQ is the added difficulty of analyzing the NMR spectrum and parameterizing the internal Hamiltonian [34, 102, 103].

An additional challenge arises due to the relatively small differences in nuclear spin resonance frequencies in an LNQ. For a molecule in a liquid crystal solvent, chemically distinct nuclear spins are distinguishable by their resonance frequencies  $\nu_j$ . However, the chemical shift differences  $\Delta\nu_{jk} = |\nu_j - \nu_k|$  may be very small, and the time required to distinguish among the spins is proportional to  $1/\Delta\nu_{jk}$ . Consequently, control sequences which distinguish among the spins are long in time, negating the enhancement in computing speed enabled by strong dipolar couplings and augmenting the effects of decoherence. This challenge is addressed in Chapter Five of this thesis by encoding logical qubits in a decoherence free subspace (DFS). Logical qubit rotations are implemented by the dipolar interaction and need not distinguish the resonance frequencies of the nuclear spins, which allows shorter control sequences [31]. In addition, by storing quantum information in a DFS, the effects of decoherence are minimized, as the state of the logical qubits is immune to certain types of noise [32, 70, 122].

**Prior work with LNQs** The potential advantages of an LNQ were first demonstrated in an implementation of the Grover search algorithm using partially oriented chloroform [120]. Since then, more complex systems have been explored. LNQs have been used to implement adiabatic quantum algorithms [79], entangled states [76], universal coherent control [72], quantum information processing with spins greater than 1/2 [27, 28, 56, 97], and demonstrations with up to seven nuclear spins [64]. Recent work [73] has shown the success of strongly modulating pulses [37] for coherent control of dipolar-coupled nuclear spins in an LNQ.

In previous studies of LNQs involving multiple homonuclear spins-1/2, the physical parameters of the internal Hamiltonian ( $d_{jk}$ ,  $\nu_j$ , and  $J_{jk}$ ) were not measured. Instead, a two-dimensional NMR method, HET-Z-COSY [26], identified connectivities among the eigenstates of the internal Hamiltonian, and these states were used as the computational basis of the LNQ. In some of these studies, transition selective pulses were used to implement the desired unitary evolution [26, 72]. More recent work has combined the HET-Z-COSY

method with spectral fitting procedures to determine a “guess” Hamiltonian [73], but the physical parameters of the Hamiltonian are not determined. In Chapter Five of this thesis we demonstrate control sequences that are robust to variations in Hamiltonian parameters, and high fidelity control of two logical qubits is achieved even when the Hamiltonian parameters are known with some uncertainty.



## Chapter 5

# Enhanced control by logical qubit encoding

The successful transition from quantum information processing to quantum computation will require the ability to efficiently control qubits in the presence of noise. Decoherence free subspaces (DFSs) are some of the most efficient schemes of avoiding decoherence from noise sources with underlying symmetries [32, 70, 122]. There have been considerable experimental demonstrations of coherent control in DFSs including demonstrations of multiple qubit control [13, 37, 38, 45, 49, 57, 61, 63, 80, 83]. However most examples were not the natural encodings, in that the dominant noise source was not of the proper symmetry, and the control method did not simply match the available control elements. Here we explore a DFS encoding of strongly dipolar-coupled spins where the logical encoding quite naturally fits the internal Hamiltonian structure. This work builds on the extensive theoretical investigations of DFS encoding for systems with time-dependent exchange couplings [3, 31, 119, 121]. To achieve similar internal Hamiltonian structure we employ liquid crystal solvents to partially align the spin system and to reintroduce the spin-spin dipolar coupling [34].

### 5.1 System model

Liquid crystals in a strong external magnetic field are partially ordered. This partial ordering restricts the thermal motion of molecules dissolved in the liquid crystal material, and consequently, the solute molecules have a preferred orientation, and the orientationally-

dependent intramolecular dipolar interactions

$$\mathcal{H}_{Dip} = \sum_{j < k} \frac{\pi}{2} d_{jk} \left( 2\sigma_z^j \sigma_z^k - \sigma_x^j \sigma_x^k - \sigma_y^j \sigma_y^k \right) \quad (5.1)$$

$$d_{jk} = \left( \frac{\mu_0 \hbar \gamma_j \gamma_k}{8\pi^2} \right) \left( \frac{1 - 3 \cos^2 \theta_{jk}}{r_{jk}^3} \right) \quad (5.2)$$

do not average to zero. However the translational motion of solute molecules is not restricted, and intermolecular dipolar couplings do average to zero. The resulting internal Hamiltonian for a liquid crystal solvent system is

$$\mathcal{H} = \sum_j \pi \nu_j \sigma_z^j + \sum_{j < k} \frac{\pi}{2} (J_{jk} + 2d_{jk}) \sigma_z^j \sigma_z^k + \sum_{j < k} \frac{\pi}{2} (J_{jk} - d_{jk}) \left( \sigma_x^j \sigma_x^k + \sigma_y^j \sigma_y^k \right) \quad (5.3)$$

where  $\nu_j$  is the resonance frequency of the  $j^{\text{th}}$  spin,  $d_{jk}$  is the dipolar coupling strength between spins  $j$  and  $k$ ,  $J_{jk}$  is the corresponding scalar coupling strength, and the sums are restricted to spins within the molecule. In liquid crystal solvent systems, dipolar coupling strengths can reach multiple kHz, and for a given pair of spins the dipolar coupling is typically one to two orders of magnitude larger than the scalar coupling. The resonance frequencies and scalar couplings can be directly measured using multiple pulse sequences that average out the dipolar interaction, such as the MREV-8 sequence [74, 75, 90]. The intramolecular dipolar coupling strengths for a partially ordered system are a result of the structure of the molecule as modified by the order parameters of the system [29, 34].

We are interested in the control of two logical qubits that are encoded to protect against collective  $\sigma_z$  noise. The logical subspace  $S_L$  for this encoding is the zero-quantum subspace of the Zeeman energy eigenstates

$$|00\rangle_L = |0101\rangle \quad (5.4)$$

$$|01\rangle_L = |0110\rangle \quad (5.5)$$

$$|10\rangle_L = |1001\rangle \quad (5.6)$$

$$|11\rangle_L = |1010\rangle. \quad (5.7)$$



We describe the system in terms of the following set of logical subspace Pauli operators

$$\begin{aligned}
\sigma_x^{L1} &= \frac{1}{2}(\sigma_x^1\sigma_x^2 + \sigma_y^1\sigma_y^2) & \sigma_x^{L2} &= \frac{1}{2}(\sigma_x^3\sigma_x^4 + \sigma_y^3\sigma_y^4) \\
\sigma_y^{L1} &= \frac{1}{2}(\sigma_y^1\sigma_x^2 - \sigma_x^1\sigma_y^2) & \sigma_y^{L2} &= \frac{1}{2}(\sigma_y^3\sigma_x^4 - \sigma_x^3\sigma_y^4) \\
\sigma_z^{L1} &= \sigma_z^1 - \sigma_z^2 & \sigma_z^{L2} &= \sigma_z^3 - \sigma_z^4
\end{aligned}$$

along with the identity term and the nine bipartite terms such as  $\sigma_x^{L1}\sigma_y^{L2}$ . Recently we have reported on liquid state NMR experiments to demonstrate coherent control for a Bell state with this encoding [49]. We have discussed leakage out of the logical subspace under the control operations [12], and we have described a convenient subsystem pseudopure state [13]. The liquid crystal system extends these studies by offering a new symmetry for the internal spin Hamiltonian that led us to expect that the logical encoding will be a more natural and efficient subspace for manipulating quantum information. The dipolar Hamiltonian has a portion that transforms as the exchange operator which has been shown to be particularly convenient for subsystem encodings [3, 31, 119, 121].

The goal of this work is to demonstrate three results: (1) improved quantum information processing by using logical qubits, (2) an implementation of a DFS with dipolar-coupled spins, and (3) high fidelity control even when we have limited knowledge of the system Hamiltonian. The spin system used in these studies is the four protons of o-chloronitrobenzene (CNB) dissolved in Merck ZLI-1132 liquid crystal at 600 MHz field and a temperature of 300 K. The proton spins are strongly coupled to each other, and all of the resonances are not resolved in the 1-D NMR spectrum shown in Figure 5-1. The order parameters for CNB aligned in a liquid crystal solvent have not been measured previously so we do not have this information on which to determine the internal Hamiltonian. We have made the following simple measurements to obtain reasonable estimates of the internal Hamiltonian: (1) a 1-D MREV-8 spectrum shown in Figure 5-1, and (2) 2-D correlation spectra between the chemical shifts under MREV-8 line narrowing and the full internal Hamiltonian. The MREV-8 spectrum indicates the chemical shifts, and the 2-D measurement provides a means of assigning the largest dipolar couplings to the appropriate chemical shifts. We measured the chemical shifts (in units of Hz)  $\nu_1 = 115$ ,  $\nu_2 = -234$ ,  $\nu_3 = 204$ , and  $\nu_4 = -86$  relative to an arbitrary transmitter frequency, and an incomplete set of approximate dipolar couplings (in units of Hz)  $d_{12} = -729$ ,  $d_{23} = -503$ , and

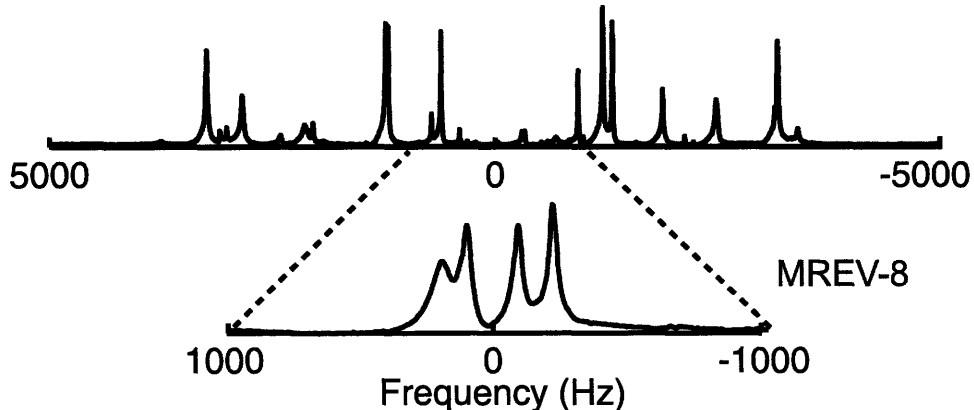


Figure 5-1: 600 MHz proton spectrum of *o*-chloronitrobenzene (CNB) partially oriented by the liquid crystal solvent ZLI-1132, where the signal due to solvent protons has been suppressed by inserting a single cycle of the Cory-48 pulse sequence before the acquisition. The inset spectrum, collected stroboscopically under the MREV-8 sequence ( $\tau = 15\mu\text{s}$ ,  $\pi/2$  pulse =  $6.85\mu\text{s}$ ), shows the four spins uncoupled with chemical shifts scaled by approximately 0.50. The spectrum after a single ( $\pi/2$ ) pulse (not shown) features a broad baseline due to the liquid crystal solvent, which contains many nonequivalent strongly dipolar-coupled protons. The baseline is suppressed in the spectra shown above because the Cory-48 pulse sequence was parameterized ( $\tau = 30\mu\text{s}$ ,  $\pi/2$  pulse =  $6.85\mu\text{s}$ ) to refocus the weaker couplings among solute protons but not the much stronger couplings among solvent protons.

$d_{34} = -1875$ . Although this limited description gives a very incomplete picture of the total system dynamics it is sufficient for our purposes.

## 5.2 Experiment

We encoded the four spin system into two logical qubits where  $d_{12}$  provided the control elements to rotate the first logical qubit,  $d_{34}$  similarly controlled the second logical qubit and  $d_{23}$  controlled the interactions between qubits. To achieve the desired control fidelity we found pulse sequences via the GRAPE algorithm [54]. Pulses were optimized for robustness to scalar couplings, the unknown dipolar couplings ( $d_{13}$ ,  $d_{14}$ ,  $d_{24}$ ), and rf inhomogeneity. The three unknown dipolar couplings were set to a distribution of values centered about a “best guess” (in units of Hz)  $d_{13} = 116$ ,  $d_{14} = -64$ , and  $d_{24} = -170$ . Although the most accurately known parameters in the internal Hamiltonian are the chemical shifts, we did not rely on them for control of the logical qubits. There is a final complication in that the three specified dipolar couplings ( $d_{12}$ ,  $d_{23}$ ,  $d_{34}$ ) are not precisely determined. We designed the control sequences to be robust against small ( $\pm 100$  Hz) variations of each of these.

The experimental goal was to create a pseudo-pure state over the logical qubits and then to entangle them in the form of a Bell state. We directly created the pseudo-pure state over the logical qubits via temporal averaging. This was accomplished in two steps. Under MREV-8 decoupling we prepared the states

$$\sigma_z^{L1} + \sigma_z^{L2} = \sigma_z^1 - \sigma_z^2 + \sigma_z^3 - \sigma_z^4 \quad (5.8)$$

$$\sigma_z^{L2} = \sigma_z^3 - \sigma_z^4 \quad (5.9)$$

relying on the differences in the chemical shifts of the four spins. To complete the pseudo-pure state preparation we used a numerically optimized GRAPE pulse to implement

$$\sigma_z^{L2} \xrightarrow{U_{prep}} \sigma_z^{L1} \sigma_z^{L2}. \quad (5.10)$$

The entangling operator we attempted to implement in the logical space is

$$U_{ent}^L = \frac{1}{\sqrt{2}} \begin{pmatrix} 1 & 0 & -i & 0 \\ 0 & -i & 0 & -1 \\ 0 & i & 0 & -1 \\ -1 & 0 & -i & 0 \end{pmatrix} \quad (5.11)$$

which takes the input state vector  $|00\rangle_L$  to the logical Bell state  $(|00\rangle_L - |11\rangle_L)/\sqrt{2}$ . A numerically optimized (GRAPE) pulse was found which performs this unitary operation over the logical subspace with high fidelity. The fidelity of the pulse, accounting for coherent errors and the uncertainty in Hamiltonian parameters, is 0.99. In addition to the preparation and entangling pulses, we found fourteen readout pulses that transform every operator in the logical space into observables. The full experiment is outlined in Fig. 5-2.

Information stored in a DFS respects a direct sum representation over the full Hilbert space. Ideal control operations over the logical qubits have the structure  $S \equiv S_L \oplus S_R$ , where  $S_L$  is the logical subspace of interest, and  $S_R$  is the remainder of the space. We attempted to prepare the initial state  $\rho_{in} = |00\rangle_L \langle 00|_L \oplus 0^R$ , where  $0^R$  is an explicit representation that the state has no component in  $S_R$ . The entangling operation over the full Hilbert space should also respect this symmetry  $U_{ent} \equiv U_{ent}^L \oplus U_{ent}^R$  where we have complete flexibility in our choice of  $U_{ent}^R$ . The challenge of course is that if the direct sum representation is

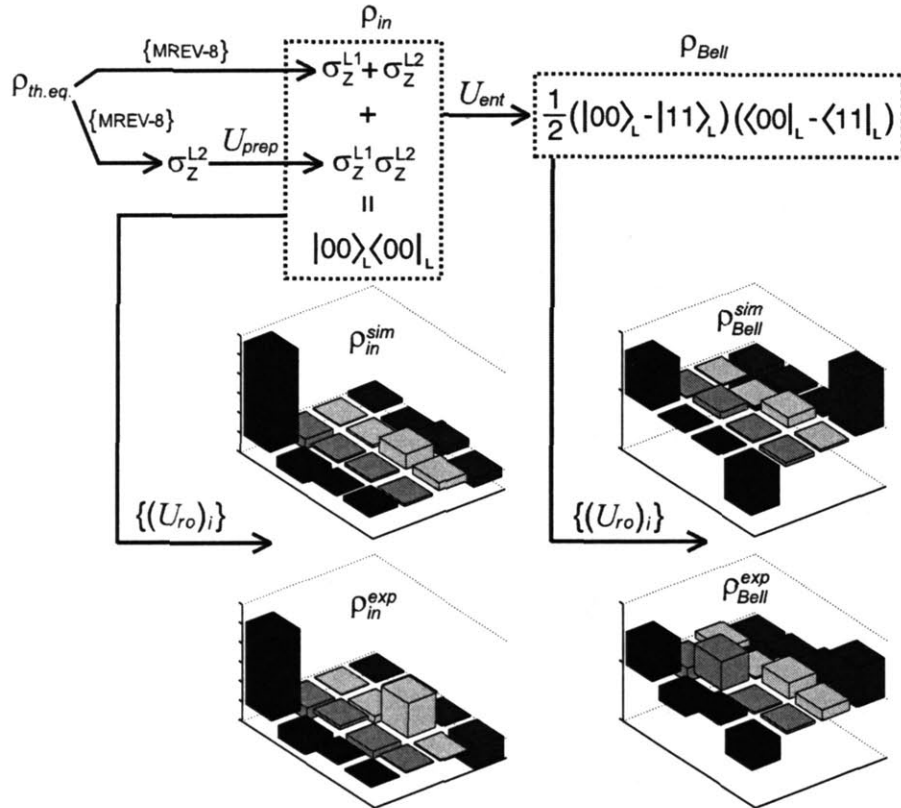


Figure 5-2: The procedure and experimental results of creating a Bell state over two logical qubits encoded in the four dipolar-coupled protons of the CNB molecule. MREV-8 sequences along with a numerically optimized preparation pulse are used to create the pseudopure input state  $|00\rangle_L$  over the logical subspace. A numerically optimized entangling operation pulse converts the input state to the logical Bell state  $(|00\rangle_L + |11\rangle_L)/\sqrt{2}$ . A set of 14 numerically optimized readout pulses were used to reconstruct the density matrices shown above. The experimentally measured logical input and Bell states have correlations of 0.90 and 0.84 (respectively) with the numerically simulated states shown above.

not maintained, the logical information can be corrupted or can leak out of the logical subspace [12, 106, 118].

$U_{prep}$  and  $U_{ent}$  were optimized over the range of dipolar couplings and rf inhomogeneity described above. The goodness function maximized by the GRAPE optimization algorithm was the logical subspace fidelity, which includes a penalty for pulses that permit leakage. The logical subspace fidelity expression is derived in Appendix A.  $U_{ent}^R$  was chosen arbitrarily. Finally, the readout pulses necessarily operated over the entire Hilbert space. They were simply designed to efficiently transform selected logical operators into observables and to be robust over the dispersion of coupling constants and rf inhomogeneity.

The reconstructed density matrices over the logical degrees of freedom are shown in Fig. 5-2. As expected, most of the observed errors arise from the initial state preparation and the readout sequences. The normalized state correlations over the logical subspace are:

$$\text{Corr}(\rho_{in}^{sim}, \rho_{in}^{exp}) = 0.90 \quad (5.12)$$

$$\text{Corr}(\rho_{Bell}^{sim}, \rho_{Bell}^{exp}) = 0.84 \quad (5.13)$$

The normalized correlations between the experimentally measured states and the ideal states are of course lower since they include more of the errors due to state preparation and readout

$$\text{Corr}(\rho_{|00\rangle_L}, \rho_{in}^{exp}) = 0.83 \quad (5.14)$$

$$\text{Corr}(\rho_{|Bell\rangle_L}, \rho_{Bell}^{exp}) = 0.76 \quad (5.15)$$

### 5.3 Analysis

To further explore the robust nature of our control over the logical subspace we have simulated the average state correlations that would be expected as the dipolar frequencies are varied. This information is shown in Figure 5-3. The loss in correlation is most pronounced for the step of creating the pseudopure state in the logical subspace. The entangling operation suffers only a small additional loss in correlation. Finally we compare our control over the encoded logical qubits to that we have over the individual spins. Figure 5-4 shows data from numerical simulations of the logical qubit entangling pulse implemented in the

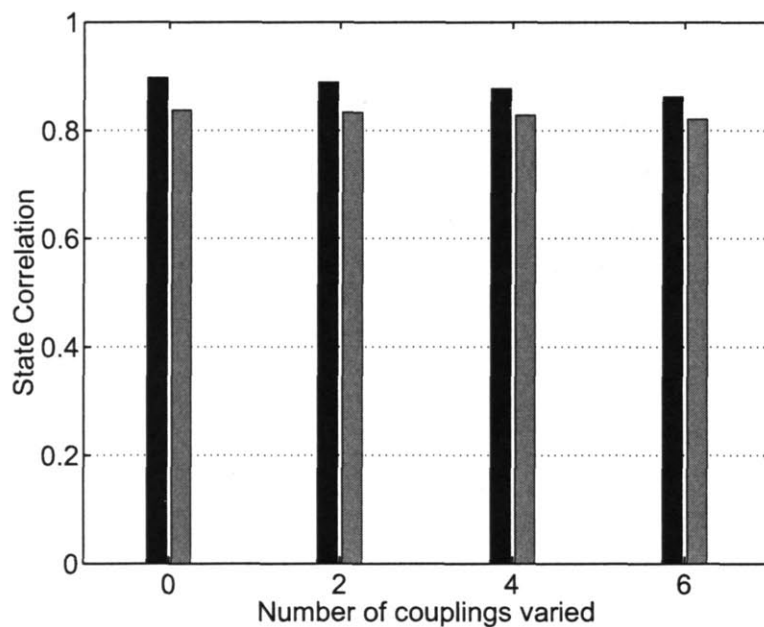


Figure 5-3: Correlation of the numerically simulated and experimentally measured density matrices for the logical input state (black) and the logical output state (green). The correlations shown are averaged over a dispersion of simulated Hamiltonian parameters. The horizontal axis indicates the number of dipolar couplings that are varied in the Hamiltonian dispersion. The individual coupling strengths are known with some uncertainty that is approximated by a dispersion centered at  $d_{jk}$  having a full width at half maximum = 200 Hz. Three points of each dispersion are sampled ( $d_{jk}$  and  $d_{jk} \pm 100$  Hz), taking only those combinations of coupling strengths that have the same sum. As more couplings are varied, the correlations decrease only slightly since the pulse sequences were engineered to be robust to these variations, and the loss in correlation is most pronounced for the input state.

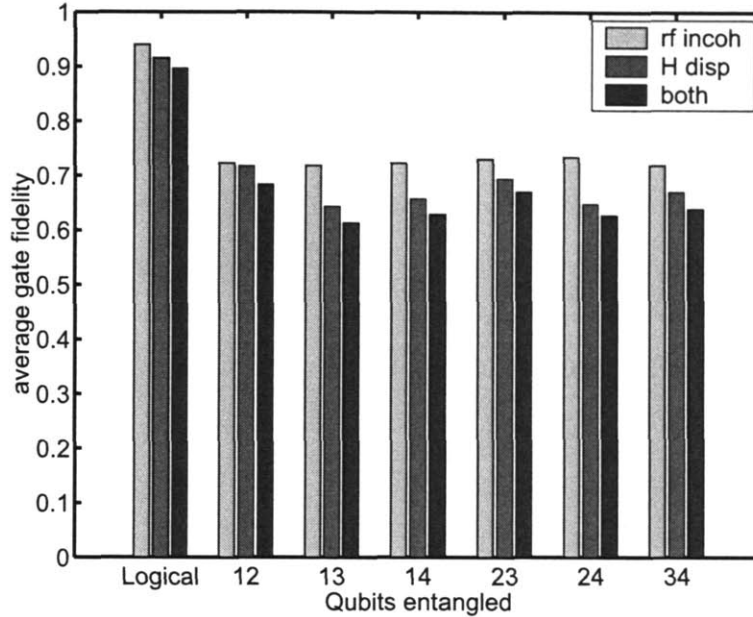


Figure 5-4: Fidelity of two-qubit entangling operation pulses numerically simulated under various conditions, comparing control of two logical qubits versus all pairs of spin qubits. The horizontal axis indicates the pair of qubits entangled. Bar color indicates the conditions of the simulation: (yellow, left) rf inhomogeneity is included in the simulation, (red, middle) a dispersion of Hamiltonians are simulated with no rf inhomogeneity, (blue, right) a dispersion of Hamiltonians are simulated with rf inhomogeneity. All fidelities are attenuated by  $\exp(-t_{pulse}/T2)$ . For logical qubits, the estimated decoherence time of the zero quantum subspace is used ( $T2=80$  ms), and for spin qubits, the longest estimated single spin decoherence time is used ( $T2=40$  ms). The fidelity under each set of conditions is significantly better in the case of logical qubits than for any pair of spin qubits.

experiment, compared to numerical simulations of the best spin qubit entangling pulses found by the same pulse optimization methods, optimizing over the full Hilbert space. The fidelity under each set of simulated conditions is significantly better in the case of logical qubits than for any pair of spin qubits.

## 5.4 Conclusions

In conclusion, we have shown that improved coherent control is achieved by encoding logical qubits in our system of four dipolar-coupled protons. Control in this system was demonstrated experimentally by creating a pseudopure state in the DFS and applying a unitary transformation to create a logical Bell state. Some of the system Hamiltonian parameters are imprecisely known, and high fidelity control was achieved by engineering pulse

sequences that are robust to these uncertainties. The structure of the system Hamiltonian for molecules dissolved in liquid crystal solvents provides a natural setting for experimental studies of logical qubit encodings. In the future, liquid crystal solvent NMR QIPs could be used to explore more complex logical encodings in larger Hilbert spaces.



# Chapter 6

## Future direction

The long-term goals of quantum computing research include the realization of scalable, fault-tolerant coherent control. This goal is motivated by the idea that quantum computers will offer exciting and unique possibilities that are not available from classical computers. In the near term, existing implementations will move toward this goal by incorporating more complexities and broader capabilities. Specifically, efforts are focused on the development of QIPs that have access to larger Hilbert spaces. Many of these ongoing experimental efforts utilize nuclear and electron spin networks in solids, where spin addressability can present an additional challenge.

Facing these challenges, a logical approach is to utilize and adapt the tools that have enabled control in smaller, less complicated systems. In this regard, liquid crystal solvent NMR QIPs (LNQs) provide a fertile ground for progress. LNQs provide modestly large Hilbert spaces for studying complex system dynamics and quantum control with limited addressability. As discussed in Chapter Four, the natural system dynamics of an LNQ are in a middle-regime, between liquid and solid state dynamics, where the tools of liquid state NMR QIP can be applied to challenges related to scalable systems.

### 6.1 Larger Hilbert spaces

In liquid state NMR QIP, the Hilbert space is defined by nuclear spins in an ensemble of molecules. Because each molecule is approximately isolated from its environment, a molecule with a small number of scalar-coupled nuclear spins creates a well-defined Hilbert space, which enables precise coherent control. In solids, nuclear spin coupling is not limited

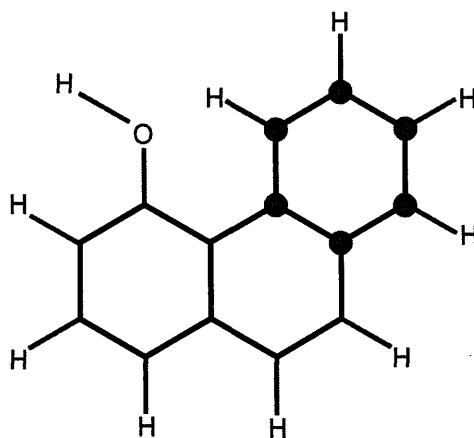


Figure 6-1: Diagram of the 4-hydroxyphenanthrene molecule which could be used as a 16 qubit heteronuclear LNQ.  $^{13}\text{C}$  labeled spins are highlighted in red. Such a system will be useful for developing control techniques in large Hilbert spaces and for exploring control in dipolar-coupled nuclear spin systems.

to nearest neighbor interactions, and each spin is coupled to many other spins by the dipolar interaction. Experiments have identified interacting spin clusters containing as many as 100 spins [18,19]. While these large spin clusters present the advantages of a large Hilbert space, approximating a well-defined, isolated Hilbert space for quantum computing is a significant challenge in these systems. Liquid crystals will enable studies in moderately large networks of dipolar-coupled spins that are small enough that the dynamics are tractable. Figure 6-1 shows a molecule that could be used for such work. Future work with molecules such as 4-hydroxyphenanthrene could help identify methods for approximating a well-defined Hilbert space within a large network of dipolar-coupled spins.

## 6.2 Limited addressability

In liquid state NMR QIP, the difference in spin resonance frequency between two spins  $\Delta\nu_{jk}$  is typically on the order of kHz, while the coupling strengths  $J_{jk}$  are typically one to two orders of magnitude smaller. In this regime, each spin-qubit is addressable by its resonance frequency, and arbitrary single-qubit manipulations are implemented by numerically optimized rf control sequences [37]. In solids,  $\Delta\nu_{jk}$  is orders of magnitude less than the dipolar coupling strength  $d_{jk}$ , and individual spins are often indistinguishable, making single spin-qubit manipulations virtually impossible.

The solution to this problem is to encode single qubits in the state of many nuclear spins, which allows single qubit manipulations to be accomplished by controlling the interaction among the spins rather than by addressing individual spin resonance frequencies [3, 31]. As demonstrated in Chapter Five, liquid crystals provide a natural setting for exploring coherent control of logical qubits. Figure 6-2 demonstrates that liquid crystals are in a regime of addressability between liquids and solids. In a liquid crystal, individual transitions are resolved in the spectrum, but individual spins are not efficiently manipulated, since the coupling strengths are comparable to and often greater than the differences in resonance frequencies  $\Delta\nu_{jk}$ . Future studies with LNQs will progress to larger spin systems, incorporating more complex logical encodings involving more than two spins per logical qubit, which provides protection from a larger class of noise generators.

### 6.3 Complex dynamics

In liquid state NMR QIPs, dipolar couplings among nuclear spins are averaged out naturally by the thermal motion of the molecules, and nuclear spins interact through scalar coupling. The interaction is often in the weak coupling regime where the coupling term  $J_{jk}\sigma^j \cdot \sigma^k$  is well approximated by  $J_{jk}\sigma_z^j\sigma_z^k$ . In such a regime, simulating a strongly mixing anisotropic Hamiltonian can require many transformations and long coupling times. In LNQs, strong dipolar couplings provide a natural setting for simulating and controlling a wider variety of Hamiltonians. As an example, the dipolar Hamiltonian can be transformed to study evolution under XY-Heisenberg couplings [14].

Many promising approaches to scalable control involve nuclear spins in the solid state, some of which incorporate electron spins via the hyperfine interaction [21, 52, 55, 62, 94, 101]. In these systems, it will be necessary to control and precisely manipulate large anisotropic coupling terms in the system Hamiltonian. LNQs provide a means for exploring control methods for such applications.

### 6.4 Conclusions

The challenge of building a quantum computer is a significant motivation to study and control complex quantum systems. Experimental methods have been developed to enable precise coherent control in liquid state NMR QIPs, and adapting these methods to solid

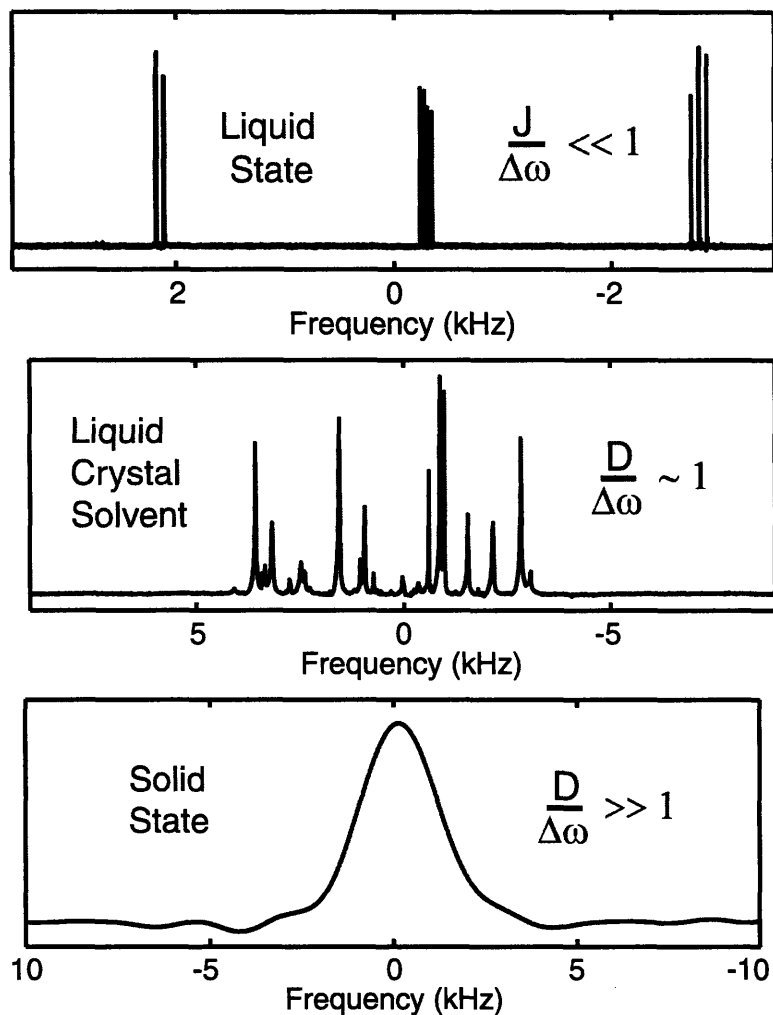


Figure 6-2: NMR spectra showing different regimes of Hamiltonians. (Top) A spectrum typical of liquid state NMR QIPs, showing three groups of peaks from three labeled  $^{13}\text{C}$  nuclei in crotonic acid. Each group of peaks is split due to scalar coupling among the spins. The couplings are orders of magnitude smaller than the chemical shift differences. (Middle) A spectrum typical of liquid crystal solvent NMR QIPs, showing many resolved peaks over a broad spectral range from the four protons of *o*-chloronitrobenzene. Each proton is strongly dipolar coupled to the three other protons. The couplings are similar in magnitude to the chemical shift differences, and individual spins are not identifiable in the spectrum. (Bottom) An NMR spectrum typical of solid state systems that have been proposed for QIPs [21, 55, 62, 94, 101], showing many  $^{29}\text{Si}$  nuclear spins, strongly coupled through the dipolar interaction in a rigid crystal lattice. Though there are many spins and many transitions in the system, a single peak, broadened by dipolar interactions, is observed.

state systems will lead to QIPs with greater capabilities. Liquid crystal solvent NMR QIPs provide a setting for this task, where the system dynamics are tractable but complex enough to present meaningful challenges and opportunities for significant progress.



# Appendix A

## Fidelity of logical qubit control

### A.1 Measures of control

In an experiment, the control sequence optimized to implement  $U_{ideal}$  is modified by experimental noise. Under a noisy implementation, the resulting state can be expressed by a Kraus decomposition of the experimentally implemented process

$$\rho_{exp} = \sum_{\mu} A_{\mu} \rho_{in} A_{\mu}^{\dagger}. \quad (\text{A.1})$$

where the  $A_{\mu}$  must satisfy

$$\sum_{\mu} A_{\mu} A_{\mu}^{\dagger} = \mathbb{1}, \quad (\text{A.2})$$

Expression (A.1) may represent a unitary operator sum for an incoherent process or any other completely positive quantum process. The experimentally implemented quantum process can also be fully described in a Liouville space representation by the superoperator  $S_{exp}$ , where

$$S_{exp} = \sum_{\mu} \bar{A}_{\mu} \otimes A_{\mu}. \quad (\text{A.3})$$

In the superoperator notation, states are represented by columnized density matrices  $|\rho\rangle$  that are formed by stacking the columns of  $\rho$  from left to right, and state evolution is expressed

$$|\rho_{exp}\rangle = S_{exp} |\rho_{in}\rangle. \quad (\text{A.4})$$

The superoperator describing a unitary process  $U$  is given by  $S = \bar{U} \otimes U$ , where the overbar denotes complex conjugation.

Typically, three measures of control are of interest in quantum computation. The correlation between two quantum states

$$C(\rho_{ideal}, \rho_{exp}) = \frac{\text{trace}(\rho_{ideal}\rho_{exp})}{\sqrt{\text{trace}(\rho_{ideal}^2)\text{trace}(\rho_{exp}^2)}} \quad (\text{A.5})$$

indicates the overlap of the two states in Hilbert space. The attenuated correlation between two quantum states

$$A(\rho_{ideal}, \rho_{exp}, \rho_{in}) = C(\rho_{ideal}, \rho_{exp}) \sqrt{\frac{\text{trace}(\rho_{exp}^2)}{\text{trace}(\rho_{in}^2)}} \quad (\text{A.6})$$

includes a penalty for loss of state purity. Finally, the fidelity of the implemented quantum process is defined

$$F = \overline{A(\rho_{ideal}, \rho_{exp}, \rho_{in})}, \quad (\text{A.7})$$

the average attenuated correlation over a complete set of input basis states (average denoted by overbar). There are multiple equivalent expressions for the fidelity. For example, as derived in [37],

$$F = \sum_{\mu} \left| \text{trace}(U_{ideal}^{\dagger} A_{\mu}) / N \right|^2, \quad (\text{A.8})$$

where  $N$  is the Hilbert space dimension. Following from equation (A.8), when the implemented process is unitary, the fidelity is given by

$$F = \left| \text{trace}(U_{ideal}^{\dagger} U_{exp}) / N \right|^2 \quad (\text{A.9})$$

When  $U_{ideal}$  is represented in the Liouville space  $S_{ideal} = \bar{U}_{ideal} \otimes U_{ideal}$  (overbar denotes complex conjugation), the fidelity is given by

$$F = \text{trace}(S_{exp}^{\dagger} S_{ideal}) / N^2 \quad (\text{A.10})$$



## A.2 Control in the logical subspace

When implementing control in a logical subspace, measures of control need to be modified. The system Hamiltonian is defined over the full Hilbert space  $S \equiv S_L \oplus S_R$ , where  $S_L$  is the logical subspace of interest, and  $S_R$  is the remainder of the space. An operator  $\mathcal{O}$  in  $S$  has a component in  $S_L$  which is extracted by the projection operation

$$\mathcal{O}^L = \sum_{jj'=1}^{N_L} |L_j\rangle \langle L_j| \mathcal{O} |L_{j'}\rangle \langle L_{j'}| \quad (\text{A.11})$$

where the  $|L_j\rangle$  form a complete set of  $N_L$  basis vectors in  $S_L$ . The component of  $\mathcal{O}$  in  $S_R$  is given similarly by

$$\mathcal{O}^R = \sum_{tt'=1}^{N_R} |R_t\rangle \langle R_t| \mathcal{O} |R_{t'}\rangle \langle R_{t'}| \quad (\text{A.12})$$

where the  $|R_t\rangle$  form a complete set of  $N_R$  basis vectors in  $S_R$ .

It is assumed that the initial state resides in  $S_L$ , such that  $\rho_{in} = \rho_{in}^L \oplus 0^R$ , where  $0^R$  is an explicit representation that the state has no component in  $S_R$ . The ideal unitary evolution has the form  $U_{ideal} \equiv U_{ideal}^L \oplus U_{ideal}^R$ , which implies that there is no leakage into  $S_R$ . This means that no instantaneous state has elements in  $S_R$ , and the final state after ideal evolution  $\rho_{ideal} = U_{ideal} \rho_{in} U_{ideal}^\dagger = \rho_{ideal}^L \oplus 0^R$  also resides in  $S_L$ .

Errors in the implementation of  $U_{ideal}$  may cause leakage into  $S_R$ . In this case, the logical component of the Kraus operators representing the noisy process  $A_\mu$  are sufficient for describing the component of the resulting state in the logical space. Given that  $\rho_{in} = \rho_{in}^L \oplus 0^R$ , the component of  $\rho_{exp}$  in  $S_L$  is

$$\rho_{out}^L = \sum_{\mu} A_{\mu}^L \rho_{in}^L A_{\mu}^{L\dagger}. \quad (\text{A.13})$$

The set of operators  $A_{\mu}^L$  contains information about errors in the logical subspace and is affected by leakage to  $S_R$ . Consequently, we are only interested in the fidelity of  $A_{\mu}^L$ , the process which affects the evolution of the component of the state in  $S_L$ . The fidelity of the process  $A_{\mu}^L$  is given by

$$F_L = \sum_{\mu} \left| \text{trace} \left( U_{ideal}^{L\dagger} A_{\mu}^L \right) / N_L \right|^2. \quad (\text{A.14})$$

$F_L$  has the three necessary qualities of a good measure of control in the logical subspace: (1)

there is a penalty for leakage out of the logical subspace, (2) there is no penalty for errors restricted to the space  $S_R$ , and (3)  $F_L$  is equivalent to the full space fidelity when errors are restricted to the logical subspace. We now prove that  $F_L$  is equivalent to the fidelity of the full Hilbert space operator  $A_\mu$  as in equation (A.8), but where the trace sum is restricted to  $S_L$ . That is to say that the quantity in equation (A.14) is equivalent to the attenuated correlation averaged over a complete set of input basis states in the logical subspace. We begin with an explicit expression of equation (A.8) with the restricted trace sum

$$F = \sum_{\mu} \left| \text{trace}_L \left( U_{ideal}^\dagger A_\mu \right) / N_L \right|^2 \quad (\text{A.15})$$

$$= \sum_{\mu} \left| \left( \sum_{j=1}^{N_L} \langle L_j | U_{ideal}^\dagger A_\mu | L_j \rangle \right) / N_L \right|^2 \quad (\text{A.16})$$

We now insert three operators which correspond to identity in the full space  $S$

$$F = \sum_{\mu} \left| \left( \sum_{j=1}^{N_L} \sum_{\{k\}=1}^N \langle L_j | k \rangle \langle k | U_{ideal}^\dagger | k' \rangle \langle k' | A_\mu | k'' \rangle \langle k'' | L_j \rangle \right) / N_L \right|^2 \quad (\text{A.17})$$

Given that  $\langle L_j | k \rangle = 0$  unless  $|k\rangle \in S_L$  and  $\langle k'' | L_j \rangle = 0$  unless  $|k''\rangle \in S_L$ , the sums over  $k$  and  $k''$  are restricted to elements in  $S_L$ , and we rewrite the expression

$$F = \sum_{\mu} \left| \left( \sum_{\{j\}=1}^{N_L} \sum_{k'=1}^N \langle L_j | L_{j'} \rangle \langle L_{j'} | U_{ideal}^\dagger | k' \rangle \langle k' | A_\mu | L_{j''} \rangle \langle L_{j''} | L_j \rangle \right) / N_L \right|^2 \quad (\text{A.18})$$

Finally, because the ideal unitary  $U_{ideal}$  does not create leakage of states from  $S_L$  to  $S_R$ , the elements of  $\langle L_{j'} | U_R | k' \rangle$  will be zero unless  $|k'\rangle \in S_L$ . Now

$$F = \sum_{\mu} \left| \left( \sum_{\{j\}=1}^{N_L} \langle L_j | L_{j'} \rangle \langle L_{j'} | U_{ideal}^\dagger | L_{j''} \rangle \langle L_{j''} | A_\mu | L_{j''} \rangle \langle L_{j''} | L_j \rangle \right) / N_L \right|^2 \quad (\text{A.19})$$

and by (A.11), this is equal to

$$F = \sum_{\mu} \left| \left( \sum_{j=1}^{N_L} \langle L_j | U_{ideal}^{L\dagger} A_\mu^L | L_j \rangle \right) / N_L \right|^2 \quad (\text{A.20})$$

which is equivalent to (A.14).

In our numerical optimization scheme in Chapter Five, we optimize over an incoherent process and a dispersion of Hamiltonians, where the dynamics for each member of the ensemble are unitary, and the operators in the sum of equation (A.13) may be expressed  $A_\mu = \sqrt{p_\mu} U_\mu$ , where  $\sum_\alpha p_\alpha = 1$ . In this case, our fidelity is given by

$$F = \sum_\alpha p_\alpha \left| \text{trace} \left( U_{ideal}^{L\dagger} U_\alpha^L \right) / N_L \right|^2 \quad (\text{A.21})$$



# Bibliography

- [1] D. S. Abrams and S. Lloyd. Simulation of many-body fermi systems on a universal quantum computer. *Physical Review Letters*, 79(13):2586–2589, Sep 1997.
- [2] D. S. Abrams and S. Lloyd. Quantum algorithm providing exponential speed increase for finding eigenvalues and eigenvectors. *Physical Review Letters*, 83(24):5162–5165, Dec 1999.
- [3] D. Bacon, J. Kempe, D. A. Lidar, and K. B. Whaley. Universal fault-tolerant quantum computation on decoherence-free subspaces. *Physical Review Letters*, 85(8):1758–1761, Aug 2000.
- [4] J. Baugh, O. Moussa, C. A. Ryan, R. Laflamme, C. Ramanathan, T. F. Havel, and D. G. Cory. Solid-state nmr three-qubit homonuclear system for quantum-information processing: Control and characterization. *Physical Review A*, 73(2):022305, 2006.
- [5] J. Baugh, O. Moussa, C. A. Ryan, A. Nayak, and R. Laflamme. Experimental implementation of heat-bath algorithmic cooling using solid-state nuclear magnetic resonance. *Nature*, 438:470–473, 2005.
- [6] G. Benenti, G. Casati, and S. Montangero. Quantum computing and information extraction for dynamical quantum systems. *Quantum Information Processing*, 3:273–293, 2004.
- [7] G. Benenti, G. Casati, S. Montangero, and D. L. Shepelyansky. Efficient quantum computing of complex dynamics. *Physical Review Letters*, 87(22):227901, 2001.
- [8] G. Benenti, G. Casati, S. Montangero, and D. L. Shepelyansky. Dynamical localization simulated on a few-qubit quantum computer. *Physical Review A*, 67(5):052312, 2003.

- [9] N. Boulant, K. Edmonds, J. Yang, M. A. Pravia, and D. G. Cory. Experimental demonstration of an entanglement swapping operation and improved control in nmr quantum-information processing. *Physical Review A*, 68(3):032305, Sep 2003.
- [10] N. Boulant, J. Emerson, T. F. Havel, D. G. Cory, and S. Furuta. Incoherent noise and quantum information processing. *Journal of Chemical Physics*, 121(7):2955–2961, 2004.
- [11] N. Boulant, L. Viola, E. M. Fortunato, and D. G. Cory. Experimental implementation of a concatenated quantum error-correcting code. *Physical Review Letters*, 94(13):130501, Apr 2005.
- [12] P. Cappellaro, J. S. Hodges, T. F. Havel, and D. G. Cory. Principles of control for decoherence-free subsystems. *Journal of Chemical Physics*, 125(4):044514, 2006.
- [13] P. Cappellaro, J. S. Hodges, T. F. Havel, and D. G. Cory. Subsystem pseudopure states. *Physical Review A*, 75(4):042321, 2007.
- [14] Paola Cappellaro. *Quantum Information Processing in Multi-Spin Systems*. PhD dissertation, Massachusetts Institute of Technology, Department of Nuclear Science and Engineering, 2006.
- [15] H. Y. Carr and E. M. Purcell. Effects of diffusion on free precession in nuclear magnetic resonance experiments. *Physical Review*, 94(3):630–638, May 1954.
- [16] G. Casati, B. V. Chirikov, F. M. Izraelev, and J. Ford. Stochastic behavior in classical and quantum hamiltonian systems. *Lecture Notes in Physics*, 93:334, 1979.
- [17] Z. Chen, J. Yezpez, and D. G. Cory. Simulation of the burgers equation by nmr quantum-information processing. *Physical Review A*, 74(4):042321, Oct 2006.
- [18] H. Cho, P. Cappellaro, D. G. Cory, and C. Ramanathan. Decay of highly correlated spin states in a dipolar-coupled solid: Nmr study of  $caf_2$ . *Physical Review B*, 74(22):224434, Dec 2006.
- [19] H. Cho, T. D. Ladd, J. Baugh, D. G. Cory, and C. Ramanathan. Multispin dynamics of the solid-state nmr free induction decay. *Physical Review B*, 72(5):054427, Aug 2005.

- [20] D. G. Cory, A. F. Fahmy, and T. F. Havel. Ensemble quantum computing by nmr spectroscopy. *Proceedings of the National Academy of Sciences of the United States of America*, 94:1634, 1997.
- [21] D. G. Cory, R. Laflamme, E. Knill, L. Viola, T. Havel, N. Boulant, G. Boutis, E. Fortunato, S. Lloyd, R. Martinez, C. Negrevergne, M. Pravia, Y. Sharf, G. Teklemariam, Y.S. Weinstein, and W.H. Zureck. NMR based quantum information processing: Achievements and prospects. *Fortschritte der Physik-progress of physics*, 48:875, 2000.
- [22] D. G. Cory, J. B. Miller, and A. N. Garroway. Time-suspension multiple-pulse sequences: applications to solid-state imaging. *Journal of Magnetic Resonance*, 90:205–213, 1990.
- [23] D. G. Cory, M. D. Price, W. Maas, E. Knill, R. Laflamme, W. H. Zurek, T. F. Havel, and S. S. Somaroo. Experimental quantum error correction. *Physical Review Letters*, 81(10):2152–2155, Sep 1998.
- [24] H. K. Cummins, G. Llewellyn, and J. A. Jones. Tackling systematic errors in quantum logic gates with composite rotations. *Physical Review A*, 67(4):042308, Apr 2003.
- [25] M. Dahleh, A. P. Peirce, and H. Rabitz. Optimal control of uncertain quantum systems. *Physical Review A*, 42(3):1065–1079, Aug 1990.
- [26] R. Das, R. Bhattacharyya, and A. Kumar. Quantum information processing by nmr using a 5-qubit system formed by dipolar coupled spins in an oriented molecule. *Journal of Magnetic Resonance*, 170(2):310–321, October 2004.
- [27] R. Das and A. Kumar. Use of quadrupolar nuclei for quantum-information processing by nuclear magnetic resonance: Implementation of a quantum algorithm. *Physical Review A*, 68(3):032304, Sep 2003.
- [28] R. Das and A. Kumar. Experimental implementation of a quantum algorithm in a multiqubit nmr system formed by an oriented  $7/2$  spin. *Applied Physics Letters*, 89:024107, 2006.
- [29] P. Diehl and C. Khetrpal. *NMR Basic Principles and Progress, Vol. 1*. Springer-Verlag, Berlin, 1969.

- [30] D. P. DiVincenzo. The physical implementation of quantum computation. *Fortschritte der physik-progress of physics*, 48:771–783, 2000.
- [31] D. P. DiVincenzo, D. Bacon, J. Kempe, G. Burkard, and K. B. Whaley. Universal quantum computation with the exchange interaction. *Nature*, 408:339–342, 2000.
- [32] L.-M. Duan and G.-C. Guo. Preserving coherence in quantum computation by pairing quantum bits. *Physical Review Letters*, 79(10):1953–1956, Sep 1997.
- [33] J. Emerson, Y. S. Weinstein, S. Lloyd, and D. G. Cory. Fidelity decay as an efficient indicator of quantum chaos. *Physical Review Letters*, 89(28):284102, Dec 2002.
- [34] J. W. Emsley and J. C. Lindon. *NMR Spectroscopy Using Liquid Crystal Solvents*. Pergamon, Oxford, 1975.
- [35] R. R. Ernst, G. Bodenhausen, and A. Wokaun. *Principles of Nuclear Magnetic Resonance in One and Two Dimensions*. Clarendon Press, Oxford, 1987.
- [36] R. P. Feynman. Simulating physics with computers. *International Journal of Theoretical Physics*, 21(6-7):467–488, 1981/82.
- [37] E. M. Fortunato, M. A. Pravia, N. Boulant, G. Teklemariam, T. F. Havel, and D. G. Cory. Design of strongly modulating pulses to implement precise effective hamiltonians for quantum information processing. *Journal of Chemical Physics*, 116(17):7599–7606, 2002.
- [38] E. M. Fortunato, L. Viola, M. A. Pravia, E. Knill, R. Laflamme, T. F. Havel, and D. G. Cory. Exploring noiseless subsystems via nuclear magnetic resonance. *Physical Review A*, 67(6):062303, Jun 2003.
- [39] B. Georgeot and D. L. Shepelyansky. Exponential gain in quantum computing of quantum chaos and localization. *Physical Review Letters*, 86(13):2890–2893, Mar 2001.
- [40] B. Georgeot and D. L. Shepelyansky. Stable quantum computation of unstable classical chaos. *Physical Review Letters*, 86(23):5393–5396, Jun 2001.
- [41] N. A. Gershenfeld and I. L. Chuang. Bulk spin-resonance quantum computation. *Science*, 275(5298):350–356, 1997.



- [42] L. K. Grover. Quantum mechanics helps in searching for a needle in a haystack. *Physical Review Letters*, 79(2):325–328, Jul 1997.
- [43] U. Haeberlen. *High Resolution NMR in Solids: Selective Averaging*. Academic Press Inc., 1976.
- [44] U. Haeberlen and J. S. Waugh. Coherent averaging effects in magnetic resonance. *Physical Review*, 175(2):453–467, Nov 1968.
- [45] H. Haffner, F. Schmidt-Kaler, W. Hansel, C. F. Roos, T. Kober, M. Chwalla, M. Riebe, J. Benhelm, U. D. Rapol, C. Becher, and R. Blatt. Robust entanglement. *Applied Physics B: Lasers and Optics*, 81:151, 2005.
- [46] E. L. Hahn. Spin echoes. *Physical Review*, 80(4):580–594, 1950.
- [47] T. F. Havel. Robust procedures for converting among lindblad, kraus and matrix representations of quantum dynamical semigroups. *Journal of Mathematical Physics*, 44:534, 2003.
- [48] M. K. Henry, J. Emerson, R. Martinez, and D. G. Cory. Localization in the quantum sawtooth map emulated on a quantum-information processor. *Physical Review A*, 74(6):062317, 2006.
- [49] J. S. Hodges, P. Cappellaro, T. F. Havel, R. Martinez, and D. G. Cory. Experimental implementation of a logical bell state encoding. *Physical Review A*, 75(4):042320, 2007.
- [50] L. M. K. Vandersypen I. L. Chuang, X Zhou, D. W. Leung, and S. Lloyd. Experimental realization of a quantum algorithm. *Nature*, 393:143–146, 1998.
- [51] Ph. Jacquod, P.G. Silvestrov, and C.W.J. Beenakker. Golden rule decay versus lyapunov decay of the quantum loschmidt echo. *Physical Review E*, 64(5):055203, Oct 2001.
- [52] B. E. Kane. A silicon-based nuclear spin quantum computer. *Nature*, 393:133–137, 1998.
- [53] H. Kessemeier and W.-K. Rhim. Nmr line narrowing by means of rotary spin echoes. *Physical Review B*, 5(3):761–768, Feb 1972.

- [54] N. Khaneja, T. Reiss, C. Kehlet, T. Schulte-Herbruggen, and S. J. Glaser. Optimal control of coupled spin dynamics: design of nmr pulse sequences by gradient ascent algorithms. *Journal of Magnetic Resonance*, 172(2):296–305, 2005.
- [55] A. K. Khitrin, V. L. Ermakov, and B. M. Fung. Information storage using a cluster of dipolar-coupled spins. *Chemical Physics Letters*, 360:161–166, 2002.
- [56] A. K. Khitrin and B. M. Fung. Nuclear magnetic resonance quantum logic gates using quadrupolar nuclei. *Journal of Chemical Physics*, 112:6963, 2000.
- [57] D. Kielpinski, V. Meyer, M. A. Rowe, C. A. Sackett, W. M. Itano, C. Monroe, and D. J. Wineland. A decoherence-free quantum memory using trapped ions. *Science*, 291:1013–1015, 2001.
- [58] E. Knill, R. Laflamme, and L. Viola. Theory of quantum error correction for general noise. *Physical Review Letters*, 84(11):2525–2528, Mar 2000.
- [59] E. Knill, R. Laflamme, and W. H. Zurek. Resilient quantum computation. *Science*, 279:342–345, 1998.
- [60] K. Kraus. *States, Effects, and Operations*. Springer, Berlin, FRG, 1983.
- [61] P. G. Kwiat, A. J. Berglund, J. B. Altepeter, and A. G. White. Experimental verification of decoherence-free subspaces. *Science*, 290:498–501, 2000.
- [62] T. D. Ladd, J. R. Goldman, F. Yamaguchi, Y. Yamamoto, E. Abe, and K. M. Itoh. All-silicon quantum computer. *Physical Review Letters*, 89(1):017901, Jun 2002.
- [63] C. Langer, R. Ozeri, J. D. Jost, J. Chiaverini, B. DeMarco, A. Ben-Kish, R. B. Blakestad, J. Britton, D. B. Hume, W. M. Itano, D. Leibfried, R. Reichle, T. Rosenband, T. Schaetz, P. O. Schmidt, and D. J. Wineland. Long-lived qubit memory using atomic ions. *Physical Review Letters*, 95(6):060502, 2005.
- [64] J. S. Lee and A. K. Khitrin. Resurrection of schrodinger’s cat. *New Journal of Physics*, 8:144, 2006.
- [65] J. W. Lee and D. L. Shepelyansky. Quantum chaos algorithms and dissipative decoherence with quantum trajectories. *Physical Review E*, 71(5):056202, 2005.

- [66] B. Levi and B. Georgeot. Quantum computation of a complex system: The kicked harper model. *Physical Review E*, 70(5):056218, 2004.
- [67] B. Levi, B. Georgeot, and D. L. Shepelyansky. Quantum computing of quantum chaos in the kicked rotator model. *Physical Review E*, 67(4):046220, 2003.
- [68] M. Levitt. Composite pulses. *Progress in Nuclear Magnetic Resonance Spectroscopy*, 18:61, 1986.
- [69] D. A. Lidar and O. Biham. Simulating ising spin glasses on a quantum computer. *Physical Review Letters*, 56(3):3661–3681, Sep 1997.
- [70] D. A. Lidar, I. L. Chuang, and K. B. Whaley. Decoherence-free subspaces for quantum computation. *Physical Review Letters*, 81(12):2594–2597, Sep 1998.
- [71] S. Lloyd. Universal quantum simulators. *Science*, 273(5278):1073–1078, 1996.
- [72] T. S. Mahesh, N. Sinha, K. V. Ramanathan, and A. Kumar. Ensemble quantum-information processing by nmr: implementation of gates and the creation of pseudopure states using dipolar coupled spins as qubits. *Physical Review A*, 65(2):022312, Jan 2002.
- [73] T. S. Mahesh and D. Suter. Quantum-information processing using strongly dipolar coupled nuclear spins. *Physical Review A*, 74(6):062312, 2006.
- [74] P. Mansfield. Symmetrized pulse sequences in high resolution nmr in solids. *Journal of Physics C: Solid State Physics*, 4(11):1444–1452, 1971.
- [75] P. Mansfield, M. J. Orchard, D. C. Stalker, and K. H. B. Richards. Symmetrized multipulse nuclear-magnetic-resonance experiments in solids: Measurement of the chemical-shift shielding tensor in some compounds. *Physical Review B*, 7(1):90, Jan 1973.
- [76] M. Marjanska, I. L. Chuang, and M. G. Kubinec. Demonstration of quantum logic gates in liquid crystal nuclear magnetic resonance. *Journal of Chemical Physics*, 112(11):5095–5099, 2000.
- [77] Michael Mehring. *Principle of High Resolution NMR in Solids*. Springer-Verlag, 1983.

- [78] S. Meiboom and D. Gill. Modified spin-echo method for measuring nuclear relaxation times. *Review of Scientific Instruments*, 29(8):688–691, 1958.
- [79] A. Mitra, A. Ghosh, R. Das, A. Patel, and A. Kumar. Experimental implementation of local adiabatic evolution algorithms by an nmr quantum information processor. *Journal of Magnetic Resonance*, 177:285–298, 2005.
- [80] M. Mohseni, J. S. Lundeen, K. J. Resch, and A. M. Steinberg. Experimental application of decoherence-free subspaces in an optical quantum-computing algorithm. *Physical Review Letters*, 91(18):187903, Oct 2003.
- [81] C. Negrevergne, T. S. Mahesh, C. A. Ryan, M. Ditty, F. Cyr-Racine, W. Power, N. Boulant, T. Havel, D. G. Cory, and R. Laflamme. Benchmarking quantum control methods on a 12-qubit system. *Physical Review Letters*, 96(17):170501, May 2006.
- [82] M. A. Nielsen and I. L. Chuang. *Quantum Computation and Quantum Information Processing*. Cambridge University Press, Cambridge, 2000.
- [83] Jason E. Ollerenshaw, Daniel A. Lidar, and Lewis E. Kay. Magnetic resonance realization of decoherence-free quantum computation. *Phys. Rev. Lett.*, 91(21):217904, Nov 2003.
- [84] E. Ott, T. M. Antonsen, and J. D. Hanson. Effect of noise on time-dependent quantum chaos. *Physical Review Letters*, 53(23):2187–2190, 1984.
- [85] A. P. Peirce, M. A. Dahleh, and H. Rabitz. Optimal control of quantum-mechanical systems: Existence, numerical approximation, and applications. *Physical Review A*, 37(12):4950–4964, Jun 1988.
- [86] A. Peres. Stability of quantum motion in chaotic and regular systems. *Physical Review A*, 30(4):1610–1615, Oct 1984.
- [87] J. G. Powles and P. Mansfield. Double-pulse nuclear-resonance transients in solids. *Physics Letters*, 2:58, 1962.
- [88] M. A. Pravia, N. Boulant, J. Emerson, A. Farid, E. M. Fortunato, T. F. Havel, R. Martinez, and D. G. Cory. Robust control of quantum information. *Journal of Chemical Physics*, 119(19):9993–10001, 2003.

- [89] C. Ramanathan, S. Sinha, J. Baugh, T. F. Havel, and D. G. Cory. Selective coherence transfers in homonuclear dipolar coupled spin systems. *Physical Review A*, 71(2):020303, Feb 2005.
- [90] W-K. Rhim, D. D. Elleman, and R. W. Vaughan. Analysis of multiple pulse nmr in solids. *Journal of Chemical Physics*, 59(7):3740–3749, 1973.
- [91] W.-K. Rhim and H. Kessemeier. Transverse-magnetization recovery in the rotating frame. *Physical Review B*, 3(11):3655–3661, Jun 1971.
- [92] W-K. Rhim, A. Pines, and J. S. Waugh. Time-reversal experiments in dipolar-coupled spin systems. *Physical Review B*, 3(3):684–696, Feb 1971.
- [93] R. Schack. Using a quantum computer to investigate quantum chaos. *Physical Review A*, 57(3):1634–1635, Mar 1998.
- [94] M. S. Shahriar, P. R. Hemmer, S. Lloyd, P. S. Bhatia, and A. E. Craig. Solid-state quantum computing using spectral holes. *Physical Review A*, 66(3):032301, Sep 2002.
- [95] P. W. Shor. Algorithms for quantum computation: Discrete logarithms and factoring. *Proceedings of the 35th Annual Symposium on Foundations of Computer Science*, pages 124 – 134, 1994.
- [96] P. W. Shor. Scheme for reducing decoherence in quantum computer memory. *Physical Review A*, 52(4):R2493–R2496, Oct 1995.
- [97] N. Sinha, T. S. Mahesh, K. V. Ramanathan, and A. Kumar. Toward quantum information processing by nuclear magnetic resonance: Pseudopure states and logical operations using selective pulses on an oriented spin 3/2 nucleus. *Journal of Chemical Physics*, 114(10):4415–4420, 2001.
- [98] S. Somaroo, C. H. Tseng, T. F. Havel, R. Laflamme, and D. G. Cory. Quantum simulations on a quantum computer. *Physical Review Letters*, 82(26):5381–5384, Jun 1999.
- [99] P. H. Song and D. L. Shepelyansky. Quantum computing of quantum chaos and imperfection effects. *Physical Review Letters*, 86(10):2162–2165, 2001.

- [100] A. M. Steane. Error correcting codes in quantum theory. *Physical Review Letters*, 77(5):793–797, Jul 1996.
- [101] D. Suter and K. Lim. Scalable architecture for spin-based quantum computers with a single type of gate. *Physical Review A*, 65(5):052309, Apr 2002.
- [102] R. T. Syvitski, N. Burlinson, E. E. Burnell, and J. Jeener. Simultaneous selective detection of multiple quantum spectra. *Journal of Magnetic Resonance*, 155:251–256, 2002.
- [103] R. T. Syvitski and E. E. Burnell. Multiple quantum and high-resolution nmr, molecular structure, and order parameters of partially oriented ortho and meta dimethyl-, dichloro-, and chloromethylbenzenes codissolved in nematic liquid crystals. *Journal of Magnetic Resonance*, 144:58–73, 2000.
- [104] G. Teklemariam, E. M. Fortunato, M. A. Pravia, T. F. Havel, and D. G. Cory. Nmr analog of the quantum disentanglement eraser. *Physical Review Letters*, 86(26):5845–5849, 2001.
- [105] G. Teklemariam, E. M. Fortunato, M. A. Pravia, Y. Sharf, T. F. Havel, D. G. Cory, A. Bhattaharyya, and J. Hou. Quantum erasers and probing classifications of entanglement via nuclear magnetic resonance. *Physical Review A*, 66(1):012309, Jul 2002.
- [106] L. Tian and S. Lloyd. Resonant cancellation of off-resonant effects in a multilevel qubit. *Physical Review A*, 62(5):050301, Oct 2000.
- [107] C. H. Tseng, S. Somaroo, Y. Sharf, E. Knill, R. Laflamme, T. F. Havel, and D. G. Cory. Quantum simulation of a three-body-interaction hamiltonian on an nmr quantum computer. *Physical Review A*, 61(1):012302, Dec 1999.
- [108] L.M.K. Vandersypen, M. Steffen, G. Breyta, C.S. Yannoni, M.H. Sherwood, and I.L. Chuang. Experimental realization of shor’s quantum factoring algorithm using nuclear magnetic resonance. *Nature*, 414:883–887, 2001.
- [109] L. Viola. Quantum control via encoded dynamical decoupling. *Physical Review A*, 66(1):012307, Jul 2002.

- [110] L. Viola, E. M. Fortunato, M. A. Pravia, E. Knill, R. Laflamme, and D. G. Cory. Experimental realization of noiseless subsystems for quantum information processing. *Science*, 293(5537):2059–2063, 2001.
- [111] L. Viola, E. Knill, and S. Lloyd. Dynamical decoupling of open quantum systems. *Physical Review Letters*, 82(12):2417–2421, Mar 1999.
- [112] L. Viola and S. Lloyd. Dynamical suppression of decoherence in two-state quantum systems. *Physical Review A*, 58(4):2733–2744, Oct 1998.
- [113] L. Viola, S. Lloyd, and E. Knill. Universal control of decoupled quantum systems. *Physical Review Letters*, 83(23):4888–4891, Dec 1999.
- [114] W. S. Warren. The usefulness of nmr quantum computing. *Science*, 277:1688–1690, 1997.
- [115] Y. S. Weinstein, T. F. Havel, J. Emerson, N. Boulant, M. Saraceno, S. Lloyd, and D. G. Cory. Quantum process tomography of the quantum fourier transform. *Journal of Chemical Physics*, 121(13):6117–6133, 2004.
- [116] Y. S. Weinstein, S. Lloyd, J. Emerson, and D. G. Cory. Experimental implementation of the quantum baker’s map. *Physical Review Letters*, 89(15):157902, Sep 2002.
- [117] Y. S. Weinstein, M. A. Pravia, E. M. Fortunato, S. Lloyd, and D. G. Cory. Implementation of the quantum fourier transform. *Physical Review Letters*, 86(9):1889–1891, 2001.
- [118] L.-A. Wu, M. S. Byrd, and D. A. Lidar. Efficient universal leakage elimination for physical and encoded qubits. *Physical Review Letters*, 89(12):127901, Aug 2002.
- [119] L.-A. Wu and D. A. Lidar. Power of anisotropic exchange interactions: Universality and efficient codes for quantum computing. *Physical Review A*, 65(4):042318, Apr 2002.
- [120] C. S. Yannoni, M. H. Sherwood, D. C. Miller, I. L. Chuang, L. M. K. Vandersypen, and M. G. Kubinec. Nuclear magnetic resonance quantum computing using liquid crystal solvents. *Applied Physics Letters*, 75(22):3563–3565, 1999.

- [121] P. Zanardi and S. Lloyd. Universal control of quantum subspaces and subsystems. *Physical Review A*, 69(2):022313, 2004.
- [122] P. Zanardi and M. Rasetti. Noiseless quantum codes. *Physical Review Letters*, 79(17):3306–3309, Oct 1997.